

1 **Assessing the ability of the ECMWF seasonal prediction model to forecast extreme**
2 **September-to-November rainfall events over Equatorial Africa**

3
4 **Hermann N. Nana^{1*} · Roméo S. Tanessong^{2,1} · Masilin Gudoshava³ · Derbetini A.**
5 **Vondou¹**

6
7 ¹Laboratory for Environmental Modelling and Atmospheric Physics (LEMAP), Physics
8 Department, University of Yaounde 1, PO Box 812, Yaounde (Cameroon)

9
10 ²Department of Meteorology and Climatology; Higher Institute of Agriculture, Forestry,
11 Water and Environment; University of Ebolowa, PO Box 118, Ebolowa (Cameroon)

12
13 ³IGAD Climate Prediction and Applications Centre (ICPAC), Nairobi, (Kenya)

14
15
16 * Corresponding author: Hermann N. Nana (nanahermann100@yahoo.com)

17
18 Hermann N. Nana's orcid: <https://orcid.org/0000-0002-0973-8613>

19
20 Roméo S. Tanessong's orcid: <https://orcid.org/0000-0003-3804-5901>

21
22 Masilin Gudoshava's orcid: <https://orcid.org/0000-0003-0315-9271>

23
24 Derbetini A. Vondou's orcid: <https://orcid.org/0000-0002-8681-5328>

25
26
27
28
29
30
31
32
33
34
35
36
37
38
39
40
41
42

43 **Abstract**

44

45 This study investigates the predictability of rainfall over Equatorial Africa (EA)
46 and evaluates the forecasting performance of the European Centre for Medium-Range
47 Weather Forecasts fifth-generation seasonal forecast version 5.1 (ECMWF-SEAS5.1) for
48 the September–November (SON) period during 1981–2023 (43 years). The analysis
49 considers two lead-times, focusing on initial conditions (ICs) from September and
50 August. Regression, spatiotemporal and composite analyses are applied to highlight
51 the relationship between extreme precipitation events over EA and the various
52 associated atmospheric circulation drivers. The analysis reveals that ECMWF-SEAS5.1
53 successfully reproduces the observed annual precipitation cycle and seasonal spatial
54 pattern of rainfall over the region for both ICs, with notably better skills for September.
55 In addition, the model effectively captures the teleconnections between EA rainfall and
56 tropical sea surface temperature, including the Indian Ocean dipole and El Niño-
57 Southern Oscillation, for both ICs. Regions with highest potential predictability skills
58 coincide with regions where the model accurately represents strong (weak) composite
59 rainfall anomalies, associated with strong (weak) moisture flux convergence
60 (divergence) values, although the magnitude tends to be underestimated. However,
61 other important observed features, such as the components of the African easterly jet,
62 are well represented by the model for the September IC, but not for August. While
63 many atmospheric mechanisms driving precipitation in the region are well simulated,
64 their underestimation likely explains the model’s general tendency to underestimate
65 the magnitude of extreme rainfall events. The results of this study support efforts to
66 improve forecast outputs in the national weather services across the region by
67 integrating ECMWF model outputs into operational weather bulletins.

68

69 **Keywords:** Equatorial Africa rainfall, Seasonal forecasting, ENSO, IOD, forecast Skill

70

71

72

73

74

75

76

77

78

79

80

81

82

83

84

85

86

87 **1. Introduction**

88

89 Equatorial Africa (EA) exhibits a complex annual rainfall cycle shaped by the
90 seasonal migration of the Intertropical Convergence Zone (ITCZ), local convection, and
91 moisture transport from the Atlantic and Indian Oceans. Among the different seasons,
92 September to November (SON) is particularly important, as it marks one of the peak
93 rainfall periods for many EA countries and is frequently associated with severe
94 hydrometeorological hazards such as floods and landslides (Moihamette et al., 2024;
95 Gudoshava et al., 2022a; Kenfack et al., 2025; Nana et al., 2025). Understanding and
96 predicting SON rainfall variability is therefore critical for risk preparedness and climate-
97 sensitive planning across the region. The SON rainfall system in EA is influenced by a
98 combination of local, regional, and large-scale drivers. Local factors include mesoscale
99 convective systems and interactions between topography and atmospheric flow
100 (Pokam et al., 2013). Regional circulation patterns, particularly over the eastern
101 equatorial Atlantic and western Indian Ocean, further modulate moisture availability
102 (Kuate et al., 2019; Longandjo and Rouault, 2020). At larger scales, Sea Surface
103 Temperature (SST) variability in the Pacific, Indian, and Atlantic oceans plays a central
104 role in shaping interannual rainfall anomalies (Pokam et al., 2014; Nicholson, 2015). In
105 particular, El Niño Southern Oscillation (ENSO), the Indian Ocean Dipole (IOD), and
106 Atlantic SST anomalies have been shown to influence SON precipitation extremes
107 across EA (Preethi et al., 2015; Roy et al., 2024; Palmer et al., 2023; Nana et al., 2025).
108 Years characterised by the co-occurrence of a positive IOD and strong El Niño such as
109 1997 and 2023 have produced widespread heavy rainfall over several EA regions
110 (Okoola et al., 2008; Nana et al., 2025). These links underscore the importance of
111 accurately capturing SST-driven teleconnections and associated atmospheric
112 circulation patterns when forecasting SON rainfall.

113 Despite advances in global numerical weather prediction systems, forecasting
114 SON precipitation over EA remains a persistent challenge. Sparse observational
115 networks, limited understanding of regional climate dynamics, and model-specific
116 errors contribute to substantial uncertainties in seasonal forecasts (Tanessong et al.,
117 2017). While several studies have evaluated the skill of general circulation models over
118 EA (e.g., Feudjio et al., 2022; Nana et al., 2024; Tanessong et al., 2024), important gaps
119 remain particularly regarding the model's ability to reproduce SON extreme rainfall
120 events and their associated large-scale drivers. Most existing evaluations focus on
121 earlier SEAS5 versions or on mechanisms relevant to other seasons (e.g., MAM or JJAS),
122 thus providing an incomplete picture of SON dynamics. These studies found that EA
123 rainfall variability is mainly associated with several factors, including easterly and
124 westerly waves, tropical cyclones, the Madden-Julian Oscillation (MJO) and sea surface
125 temperature (SST) in the Atlantic, Indian and Pacific oceans. For example, Nana et al.
126 (2024) demonstrated that the ability of seasonal forecast models to predict rainfall
127 anomalies occurring over western EA during extreme South Atlantic Ocean Dipole
128 (SAOD) events depends on their skill in forecasting the relationship between rainfall
129 and SAOD, which decreases with increasing lead time. Their results showed that the
130 ECMWF seasonal forecast system 5 (SEAS5) model best captures this relationship and

131 the associated rainfall anomalies, a finding also supported by Gebrechorkos et al.
132 (2022). Similarly, Mwangi et al. (2014) evaluated SEAS5 products against data from ten
133 East African stations and found significant forecasting skill for both rainy seasons, with
134 better performance in October–December (OND) compared to March–May (MAM). The
135 ability of the SEAS5 model to simulate the drivers of extreme rainfall during MAM
136 2018–2020 over eastern EA has been **analysed** by Gudoshava et al. (2024). The findings
137 of this study indicate that the heavy rainfall events of March–May 2018 and 2020
138 coincided with an active MJO (Phases 1–4) or a tropical cyclone east of Madagascar. In
139 contrast, the low rainfall observed during the same period in 2019 was linked to
140 tropical cyclones west of Madagascar. Their study also concluded that underestimation
141 of these extreme rainfall intensities was linked to inaccurate MJO forecasts and errors
142 in tropical cyclone location and intensity. For the June–September (JJAS) season, the
143 findings of Ehsan et al. (2022) establish that the spatial and temporal patterns of
144 observed EA rainfall variability, as well as the key climatic features that drive EA
145 precipitation excesses and deficits, are successfully captured by the SEAS5 model,
146 when **initialised** in May and April. Recent analyses have begun to examine the role of
147 large-scale climate modes in shaping extreme SON rainfall, but few studies have
148 assessed how well seasonal forecast systems capture both the rainfall anomalies and
149 the underlying physical mechanisms. For example, Tefera et al. (2025) showed that
150 SEAS5 is able to capture hydroclimatic extremes linked to coupled IOD-ENSO modes
151 during the first two lead times, but their assessment did not consider the most recent
152 ECMWF system nor did it explicitly evaluate the associated atmospheric circulation
153 patterns during SON. This gap limits our understanding of the forecast system’s ability
154 to represent the processes driving extreme rainfall variability during this crucial
155 season.

156 Motivated by these limitations, the present study evaluates the performance of
157 the latest ECMWF seasonal forecasting system, SEAS5.1 (Johnson et al., 2019), in
158 simulating SON extreme rainfall events over EA using forecasts **initialised** in August
159 and September. **However, considering that the main difference between SEAS5**
160 **and SEAS5.1 is rooted in the interpolation and additional variables (see section**
161 **2.1), rather than a change in the physics, dynamics or data assimilation of the**
162 **model, therefore, no relevant differences in terms of performance between both**
163 **versions are expected.** SEAS5.1 was selected due to its demonstrated skill in
164 representing key global climate teleconnections such as ENSO and the IOD (Nana et al.,
165 2024; Tefera et al., 2025), which exert strong influence on SON precipitation **over EA**. In
166 addition to providing an updated assessment of model skill, our study explicitly
167 examines the large-scale physical mechanisms SST anomalies, moisture transport,
168 zonal and Walker circulations that accompany extreme rainfall events. This dual
169 approach offers a more comprehensive and physically grounded evaluation than
170 previous studies, thereby contributing toward improved understanding and prediction
171 of SON rainfall extremes in EA. Extreme rainfall events are among the most impactful
172 climate hazards over EA, often leading to severe flooding, infrastructure damage, and
173 socio-economic losses, yet their predictability at seasonal timescales remains limited.
174 Understanding whether a state-of-the-art seasonal forecast system can realistically

175 represent the large-scale drivers of these extremes is therefore essential. The
176 remainder of the paper is structured as follows. Section 2 describes the SEAS5.1 model,
177 the observational and reanalysis datasets, and the methodology. Section 3 presents
178 the skill assessment of SEAS5.1. Section 4 focuses on rainfall composites and
179 associated SST patterns during extreme SON years, and Section 5 **analyses** the
180 corresponding atmospheric circulation features. Section 6 concludes the study.

181

182 2. Data and methods

183 2.1. SEAS5.1 re-forecast and observational datasets

184

185 In this study, we use re-forecast data from version 5.1 of the ECMWF seasonal
186 prediction system (SEAS5.1), initiated on the 1st of September or the 1st of August for
187 the period 1981-2016, with 25 ensemble members. Our analysis focuses on the
188 September-November (SON) season, considering two initial conditions (ICs):
189 September 1st (L0) and August 1st (L1). This means that the forecasts **initialised** in
190 September correspond to L1 and L2 for October and November, respectively. Similarly,
191 the August initial conditions indicate that forecasts were **initialised** in August;
192 therefore, the forecasts for September, October, and November correspond to L1, L2,
193 and L3, respectively. The method used to extract lead times is consistent with that
194 adopted by Ehsan et al. (2021). With this definition, the initial conditions have a
195 relatively limited influence on the model outputs across the different analyses,
196 especially when compared to the dominant predictive role of oceanic conditions.
197 Monthly mean data are used throughout. **It is important to specify that SEAS5.1**
198 **initialisations for all the months (not only August and September) were used in**
199 **order to study the rainfall annual cycle (shown in Fig. 1).** To extend the study
200 period, we include forecasts for 2017-2023, using the first 25 ensemble members with
201 the same initialization dates, ensuring each sub-period contributes equally to the
202 analysis. This results in a total of 43 years (1981-2023), with 25 ensemble members per
203 year. A comprehensive explanation of the ensemble generation strategy of SEAS5.1
204 can be found in Johnson et al. (2019). These data are available from the Copernicus
205 Climate Data Store portal (<https://climate.copernicus.eu/datasets>) at a spatial
206 resolution of $1^\circ \times 1^\circ$. The data include monthly means of total precipitation (mm day^{-1}),
207 SST (K), Mean-Sea-Level Pressure (MSLP; hPa), zonal and meridional wind components
208 (m s^{-1}), and specific humidity (Kg Kg^{-1}) at seven pressure levels (1000, 925, 850, 700, 500,
209 400, and 300 hPa). From November 2022 onwards, the updated version SEAS5.1 is
210 used, which differs from the original SEAS5 mainly by the adoption of a new
211 interpolation tool and a revised 1° grid with half-degree-**centred** latitude/longitude
212 points, ensuring consistency with other Copernicus Climate Change Service seasonal
213 forecast systems. SEAS5.1 also provides an extended set of variables, including top
214 solar incoming radiation, additional fields at the 1000 hPa pressure level, and separate
215 surface and sub-surface runoff components. The underlying model physics remains
216 unchanged between the two versions.

217 As precipitation reference in this study, observed monthly precipitation data
218 from the Climate Hazards Group Infrared Precipitation with Station data (CHIRPS; Funk

219 et al., 2015) at $0.25^\circ \times 0.25^\circ$ horizontal grid spacing are adapted. Following Dinku et al.
 220 (2018), CHIRPS has been shown to feature a good relationship with station data over
 221 eastern EA at the monthly time-scale, outperforming other satellite-based products
 222 such as Tropical Applications of Meteorology using SATellite and ground-based
 223 observations (TAMSAT) and African Rainfall Climatology version 2 (ARC2). Observed
 224 SSTs are obtained from version 5 of Extended Reconstructed SST (ERSSTv5; Huang et
 225 al., 2017) at a $2^\circ \times 2^\circ$ resolution. For additional validation, we evaluate the seasonal
 226 climatologies of atmospheric circulation from SEAS5.1 against the fifth generation of
 227 European Re-Analysis (ERA5; Hersbach et al., 2020) dataset, at a horizontal (vertical)
 228 grid spacing of $0.25^\circ \times 0.25^\circ$ (37 pressure levels from 1000 to 1 hPa). ERA5 was chosen
 229 based on its demonstrated ability to represent SON extreme events and their
 230 associated dynamics and thermodynamics over East Africa (Gleixner et al., 2020; Cook
 231 and Vizu, 2021). The precipitation from the ERA5 reanalysis has been included in these
 232 figures in order to validate ERA5 with the CHIRPS reference. For consistency in
 233 comparison, both observed and reanalysis datasets are regridded to a $1^\circ \times 1^\circ$
 234 horizontal resolution based on linear interpolation and to seven pressure levels (1000,
 235 925, 850, 700, 500, 400, and 300 hPa).

236

237 2.2. Methods

238

239 The model's Potential Predictability (PP) is estimated as the ratio between
 240 external (σ_{Ext}) and internal variance (σ_{Inte}), following the methodology of Rowell et al.
 241 (1995) and Kang and Shukla (2006). The external variance (also referred to as the signal
 242 variance) represents the variance of the ensemble mean anomalies, while internal
 243 variance (or noise variance) corresponds to the average variance of the deviations of
 244 individual ensemble members from the ensemble mean. These quantities are obtained
 245 through the following calculations:

246

$$247 \quad \sigma_{Ext} = \frac{1}{N-1} \sum_{i=1}^N (P_i - \bar{P})^2, \quad (1)$$

248

$$249 \quad \sigma_{Inte} = \frac{1}{N(N-1)} \sum_{i=1}^N \sum_{j=1}^n (P_{ij} - P_i)^2, \quad (2)$$

250

$$251 \quad P_i = \frac{1}{n} \sum_{j=1}^n P_{ij} \quad (3)$$

252

$$253 \quad \bar{P} = \frac{1}{Nn} \sum_{i=1}^N \sum_{j=1}^n P_{ij} \quad (4)$$

254

$$255 \quad PP = \frac{\sigma_{Ext}}{\sigma_{Inte}} \quad (5)$$

256

257

258 where P_{ij} is the model rainfall, P_i is the ensemble mean for the i th year and \bar{P} the
259 climatology mean of all data, with $i = 1, 2, \dots, N$ ($N= 43$, the number of years) and $j = 1,$
260 $2, \dots, n$ ($n= 25$, the ensemble size). All analyses were performed separately for each of
261 the 25 ensemble members. The ensemble mean was then computed from the 25
262 members after applying all diagnostics to each individual member, including
263 correlation and regression analyses, rainfall indices, composite anomalies, moisture
264 flux, and moisture flux divergence, following the methodology of Abid et al. (2023).

265 This analysis uses two SST indices: the Niño 3.4 index (N34) and the Dipole Mode
266 Index (DMI). The N34 index, used as a proxy for the ENSO, is defined as the area-
267 averaged SST anomaly over the region 5°S – 5°N , 170° – 120°W (Trenberth, 1997). The
268 DMI (Saji et al., 1999), which represents the IOD, is calculated as the difference
269 between the area-averaged SST anomalies in the western Indian Ocean (WIO; 10°S –
270 10°N , 50° – 70°E) and the eastern Indian Ocean (EIO; 10°S – 0°N , 90° – 110°E).

271 To compute the composite anomalies, we subtract the 1981–2023 climatological
272 mean from the composites of strong or weak events, for both the model forecasts and
273 the observational data. To capture the variability of monthly rainfall over EA, the
274 probability density function (PDF) based on the Gamma distribution, identified by
275 Husak et al. (2006) as particularly appropriate for representing the asymmetric and
276 limited nature of precipitation data, is employed. In this study, it is used to illustrate
277 how the model, as well as the observations and reanalysis, represents the
278 characteristics of both extreme and mean SON season rainfall over EA during the
279 1981–2023 period. This distribution can be expressed as follows:

280

$$281 \quad f(P_i) = \frac{1}{\beta^\alpha \Gamma(\alpha)} P_i^{\alpha-1} e^{-P_i/\beta} \text{ for } P_i > 0 \quad (6)$$

282

283 where $\alpha > 0$ is the shape parameter, $\beta > 0$ is the scale parameter, P_i denotes the rainfall
284 amount, and $\Gamma(\alpha)$ is the Gamma function.

285 Using the specific humidity (q) and horizontal wind vector (V) over the
286 atmospheric column (1000–300 hPa), environmental conditions for extreme rainfall
287 events are also analysed through an assessment of moisture flux convergence $\nabla \cdot (qV)$.
288 This quantity can be further decomposed into moisture convergence ($q\nabla \cdot V$) and
289 moisture advection ($V \cdot \nabla q$), respectively, following the formulation presented by Cook
290 and Vizy (2021) and Kolstad et al. (2024), as described by the following equation:

291

$$292 \quad \langle \nabla \cdot (qV) \rangle = \langle q \nabla \cdot V \rangle + \langle V \cdot \nabla q \rangle \quad (7)$$

293

294 where V denotes the horizontal wind and q represents the specific humidity. The angle
295 brackets “ $\langle \rangle$ ” signify the vertical integral from the surface (1000 hPa) to the top (300
296 hPa) of the atmosphere column.

297

298 Based on both CHIRPS and ERA5 dataset, extreme SON season rainfall over EA
299 (8° – 50°E ; 10°S – 10°N) were identified. The EA rainfall Index (EAI) is defined by
averaging the observed SON rainfall anomalies over EA and normalising by their

300 standard deviation. Strong (weak) years are defined as those in which the common
301 CHIRPS and ERA5 EAs exceed +0.5 standard deviation (fall below -0.5 standard
302 deviation). Positive and negative composites analyses were then performed based on
303 the years identified as strong and weak, respectively. Note that the same set of years
304 was used for all observational, reanalysis, and model variables. For Pearson
305 correlation/linear regression and composite anomaly analyses of rainfall and SST,
306 statistical significance was determined using a standard two-tailed Student's t-test to
307 estimate p-values. A 5% significance level was applied throughout, with results
308 considered locally statistically significant if $p < 0.05$. It is important to note that the
309 correction of p-values due to multiple testing was not addressed, in accordance with
310 Wilks, (2016).

311

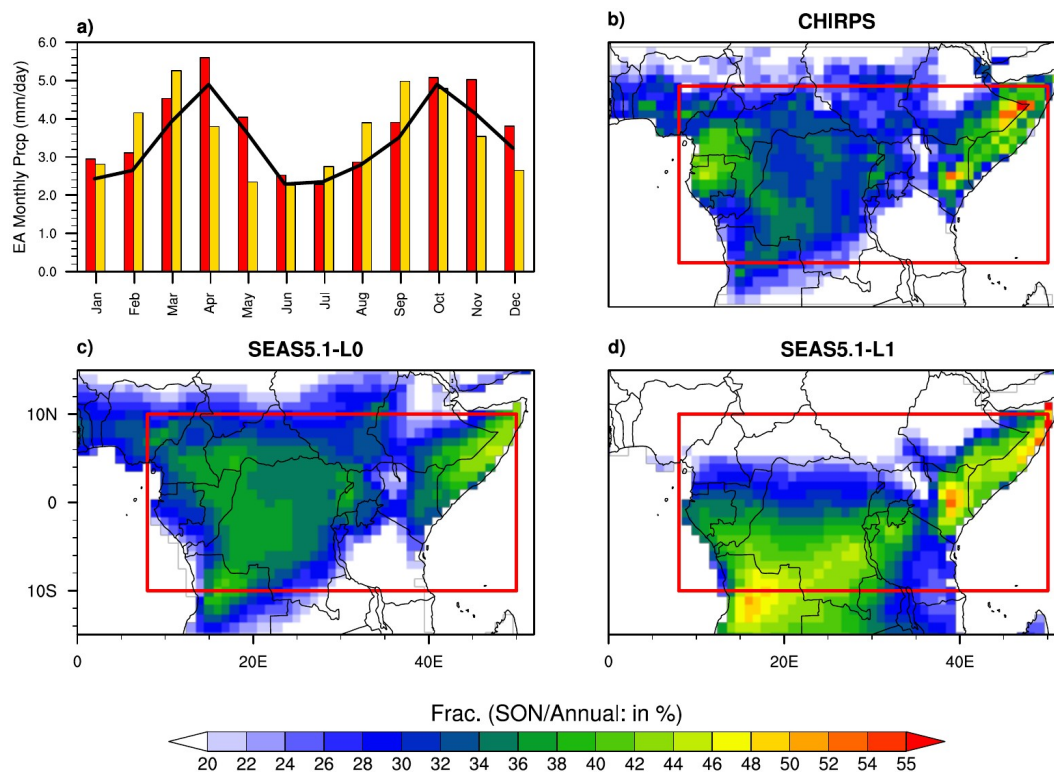
312 3. Model skills assessment

313 3.1. SEAS5.1 prediction of EA rainfall mean and variability

314

315 In this section, the model's ability to predict both monthly and SON
316 season precipitation climatology is investigated. Figure 1 illustrates the annual
317 precipitation cycle (Fig. 1a) and the precipitation fraction (Fig. 1b-d) from the CHIRPS
318 dataset and the two lead-times of SEAS5.1. For this analysis, L0 and L1 correspond to
319 the specific month and the month before, respectively. This means that June has June
320 and May as L0 and L1, respectively. Overall, the model captures the CHIRPS annual
321 rainfall cycle reasonably well, with a slight wet bias (0.2 to 0.6 mm day^{-1}) throughout the
322 year for September IC or 0-month lead-time (L0 hereafter), except in July, similar to
323 findings by Attada et al. (2022) over India. For August IC or 1-month lead-time (L1
324 hereafter), the model shows a wet bias (0.5 to 1.5 mm day^{-1}) from January to March and
325 July to September, and a dry bias (0.3 to 1 mm day^{-1}) during April to May and November
326 to December. At L1, the model fails to reproduce the observed rainfall peaks during
327 March–May (MAM) and September–December (SOND) periods, unlike L0, which
328 simulates them well. Notably, CHIRPS as well as the model at L0 both indicate rainfall
329 peaks in April and October, while at L1, the model incorrectly shifts these peaks to
330 March and September, respectively. During SON, the highest observed precipitation
331 fraction (Fig. 1b) occur over the eastern part of EA (45–50 %), mainly over south-eastern
332 Ethiopia, eastern Kenya and Somalia, as well as over Gabon and southern Cameroon
333 (40–45 %). Conversely, values drop below 20 % over Tanzania and northwest of Kenya
334 (Fig. 1b). This is consistent with findings by Gudoshava et al. (2022a,b), who also
335 showed strong (weak) rainfall contributions over southern Ethiopia, eastern Kenya and
336 Somalia (Tanzania and northwestern Kenya). The precipitation fractions forecasted at
337 L0 and L1 (Fig. 1c,d) align with the observed maximum percentages of total annual
338 precipitation occurring over eastern EA, though the model underestimates
339 (overestimates) at L0 (L1). Over western EA, SEAS5.1 slightly overestimates
340 (underestimates) the precipitation percentage over the CB (Gabon and Equatorial
341 Guinea) at L0, while at L1, it significantly overestimates (underestimates) rainfall
342 contribution over southern (northern) parts of EA.

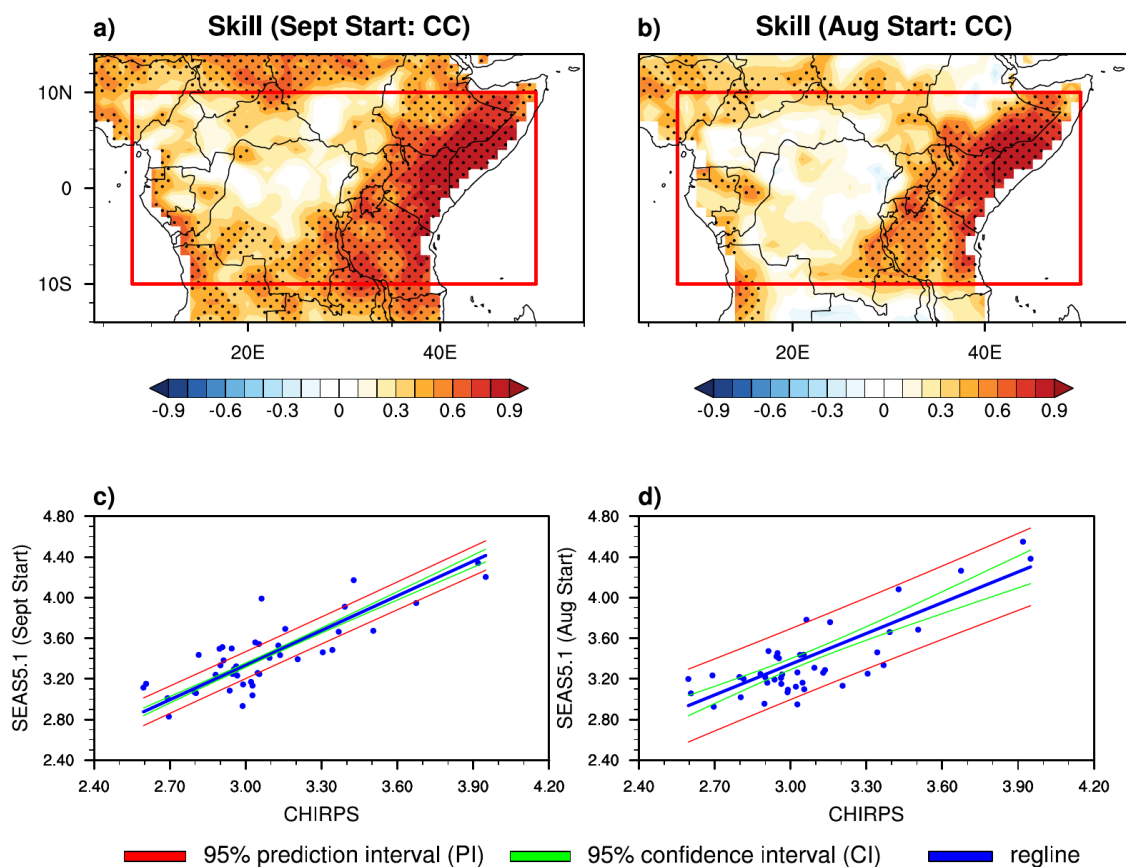
343 These results are consistent with the SON rainfall bias shown in Fig. S1a,b. At L0,
 344 the model shows a positive rainfall bias of around 3 mm day⁻¹ and negative rainfall bias
 345 of around -1 mm day⁻¹ over the CB (Gabon and Equatorial Guinea). In contrast, a larger
 346 positive bias (4 mm day⁻¹) in the southern region and a substantial negative bias (-4
 347 mm day⁻¹) in the north are observed at L1. These findings indicate that SEAS5.1
 348 performs better in simulating SON rainfall climatology over eastern EA, where both
 349 simulated error and absolute bias are less than 1 mm day⁻¹ at both lead-times (Fig. S1)
 350 compared to western EA. Furthermore, performance is generally better at L0 (bias and
 351 error around 1 mm day⁻¹) than at L1 (around 4 mm day⁻¹).



376 **Fig 1:** a) EA rainfall annual cycle comparing CHIRPS observation (black line) and SEAS5.1 over
 377 the period 1981-2023. The red (gold) bar indicates the L0 (L1) of the 25 ensemble members.
 378 Precipitation fraction [EA (SON/Annual, in %)] for b) observation, c) 0-month lead (L0) model, and
 379 d) 1-month lead (L1) model. The red boxes in b), c) and d) indicate the EA boundaries.
 380

381 In addition to the forecast skill assessment, the spatial distribution of the linear
 382 correlation coefficient (CC) between observed and simulated precipitation is shown in
 383 Fig. 2a,b to evaluate the ability of SEAS5.1 to simulate SON rainfall over EA (Nana et al.,
 384 2024). The CC value varies between - 1 and 1, where values near 0 means no predictive
 385 skill, and values approaching 1 indicate good skill. At both lead-times, a large portion
 386 of EA features strong significant and positive correlations, except over the CB, Central
 387 African Republic (CAR) and southern Cameroon. These areas with positive and
 388 significant (low and non-significant) correlation values coincide with areas where the

389 model bias and RMSE values are low and even null (strong). Overall, the model
 390 demonstrates better skill at L0 than at L1 across the region, consistent with the
 391 conclusions of Tefera et al. (2025). To further investigate the relationship between
 392 observed and predicted EA precipitation, Fig. 2c,d shows the scatter plot between
 393 CHIRPS and SEAS5.1 EA rainfall at L0 (Fig. 2c) and L1 (Fig. 2d). The red lines indicate the
 394 prediction interval (PI), while green lines indicate the confidence interval (CI). At L0, the
 395 data points, as well as the PI and CI are closer to the regression line, reflecting the
 396 strong relationship shown in Fig. 2a and the low simulated errors. Notably, the CI
 397 clearly widens as precipitation values deviate from the CHIRPS mean, indicating
 398 increasing uncertainty in the true mean as we move away from the CHIRPS mean. The
 399 PI also widens, but much more than the CI for any CHIRPS value. In contrast, at L1 (Fig.
 400 2d), the data points are more dispersed, and both the PI and CI are further away from
 401 the regression line, which is also somewhat flatter than in at L0. This finding is
 402 consistent with the low CC values observed in Fig. 2b. Similar results were reported by
 403 Ehsan et al. (2021), who also shows that the CI (linear regression line) between June-to-
 404 September Ethiopian and SEAS5 precipitation moves away from the linear regression
 405 line (bit flat) as lead-time increases.



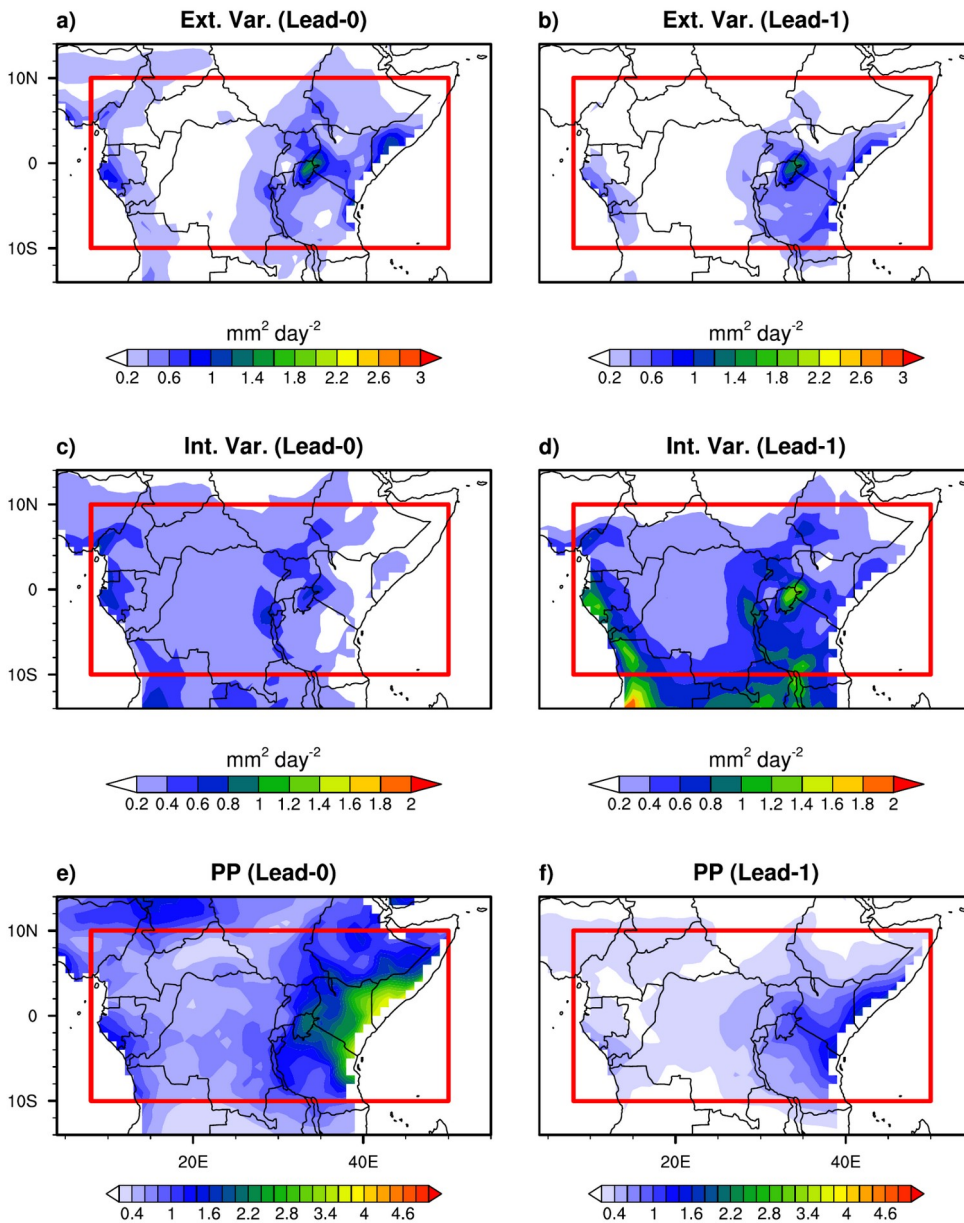
406

407 **Fig 2:** Spatial distribution of correlation coefficient (CC) between observation and ensemble
 408 mean precipitation data **initialised** in a) September, and b) August respectively. The stippling
 409 occurs where the correlation coefficient is locally statistically significant at 95% confidence level
 410 through the Student's t test. Joint plot (scatter plot) between observed (CHIRPS) and predicted

411 (SEAS5.1) EA rainfall for c) September and d) August starts for 1981-2023. Blue line is the linear
412 regression line, red (green) lines indicate the 95% prediction (confidence) interval of the model.
413 The red boxes in a) and b) indicate the EA boundaries.

414

415 The spatial distribution of both external (first row) and internal (second row)
416 variances along with the ratio (third row) of these two quantities, at L0 and L1 is
417 represented in Fig. 3. The maximum external variance values (Fig. 3a,b) occur over
418 western and eastern parts of EA at L0, with values around $1.5 \text{ mm}^2 \text{ day}^{-2}$ over eastern
419 Kenya and Somalia. However, at L1, we observe a decrease in external variance,
420 mainly over western EA, where many areas (Cameroon and Gabon) exhibit values less
421 than $0.2 \text{ mm}^2 \text{ day}^{-2}$. For the internal variance (Fig. 3c,d), the highest values occur at L1,
422 and focus over Gabon, northern Angola, western Kenya and southern Tanzania. Then,
423 the PP, as the ratio between external and internal variances is strong over coastal
424 regions, higher at L0 (Fig. 3e) compared to L1 (Fig. 3f). These maximum values (around
425 3.8 at L0 and 1.3 at L1) occur where external variance outweighs the internal variance.
426 It is noteworthy that these high values are obtained over the tropical oceanic region
427 (Eastern and south-western EA) where precipitation is strongly modulated by the
428 tropical SST, in line with the findings of Kang and Shukla (2006). These analyses show
429 that the model performs well in simulating precipitation over the region, mainly over
430 East Africa, Gabon and the western Republic of Congo. This performance is better at L0
431 than at L1 (Tefera et al., 2025). However, although the model performs well in
432 forecasting precipitation over the region during the first two lead-times, it is important
433 to assess its ability to predict the relationship between this precipitation and its main
434 drivers, the SSTs over the Indian and Pacific Oceans (Moihamette et al., 2022; Roy and
435 Troccoli 2024). The following section concerns the ability of SEAS5.1 to represent the
436 observed teleconnection.



437

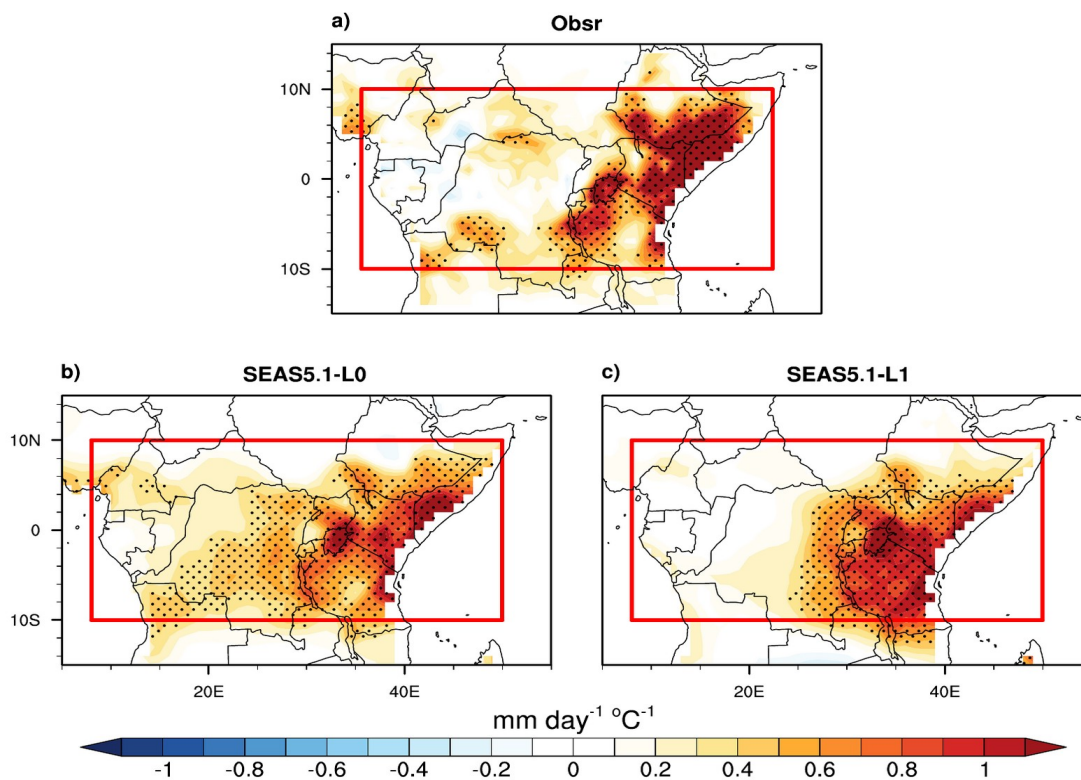
438 **Fig 3:** (a-b) External, (c-d) internal variances, and (e-f) PP for SON EA rainfall, for (first column) L0,
 439 and (second column) L1 respectively. The red boxes indicate the EA boundaries.

440

441 3.2. Physical mechanism and teleconnection patterns

442 Figure 4 shows the observed and simulated relationship through the regression
 443 analysis, between EA rainfall and the DMI. The results highlight a predominantly
 444 strong, positive and statistically significant regression between DMI and observed
 445 rainfall over the eastern part of EA (east of 30° E; Fig. 4a). Over western EA, some areas
 446 such as southern and northern DRC, and northern Angola also feature significant
 447 positive regression values. However, other regions exhibit weak (both positive and

448 negative) and even zero regression values. These findings suggest that anomalously
 449 strong rainfall over EA is generally associated with positive IOD events, characterised
 450 by warming (cooling) of SST features over the western (eastern) pole of IOD, as
 451 mentioned by Nana et al. (2025); Roy and Troccoli (2024) and Tefera et al. (2025).
 452 Conversely, an opposing rainfall pattern is observed during negative IOD episodes. The
 453 regression pattern between the predicted DMI and EA precipitation at L0 (Fig. 4b) and
 454 L1 (Fig. 4c) is quite similar to that observed. However, it is noteworthy that at L0, the
 455 model tends to underestimate (overestimated) the IOD teleconnection over eastern
 456 (western) EA regions, mainly Ethiopian (DRC and southern Cameroon) regression
 457 values. At L1, the positive relationship over eastern EA shifted southwards, with highest
 458 values over Tanzania and southern Kenya, where observed regression values were
 459 lower. This analysis suggests that the IOD-EA rainfall relationship is well captured in
 460 the model, which aligns with the findings of Nana et al. (2024), who point out that
 461 ECMWF is the best forecast model (among eleven predicting models) that captures SST-
 462 rainfall relationship over EA.

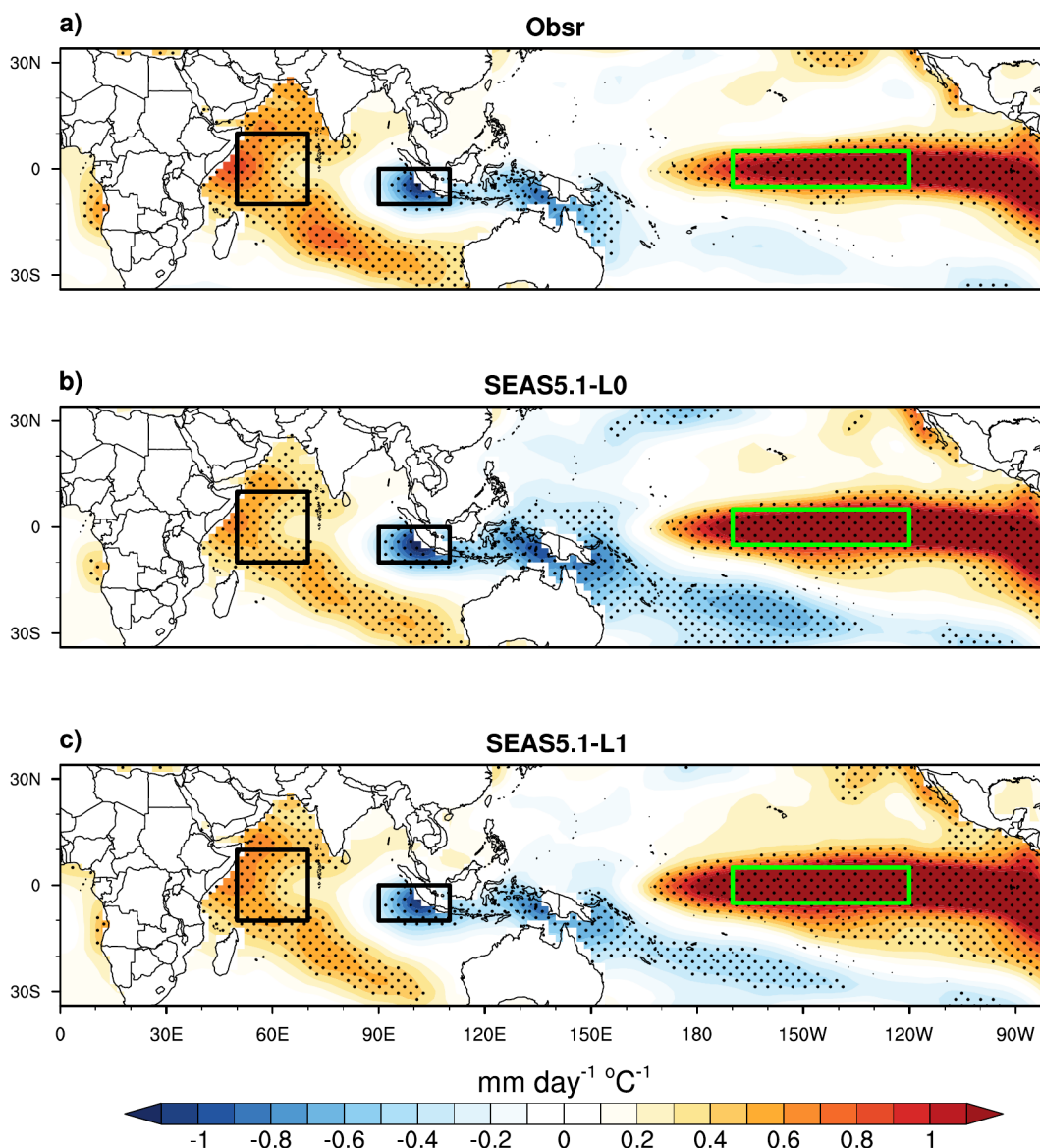


463

464 **Fig 4:** a) Regression of the DMI with the Precipitation during SON; (b) and (c) same as of (a) but
 465 for the SEAS5.1 dataset at L0 and L1, respectively. Stippling denotes where the regression is
 466 locally statistically significant at 95% confidence level. The red boxes indicate the EA boundaries.

467 Furthermore, this regression pattern between DMI and EA rainfall remains
 468 consistent when an ENSO-type signal is present over the N34 region (Fig. 5). The results
 469 support the presence of IOD-like patterns over the IO and ENSO-like patterns over the
 470 equatorial Pacific, both in observation (Fig. 5a) and model (Fig. 5b,c). Both **observation**
 471 and model exhibit significant positive (negative) regression values over WIO (EIO). The

472 equatorial Pacific highlighted here by the N3.4 index shows strong and significant
 473 positive regression (Tefera et al., 2025), suggesting that ENSO and IOD may exert over
 474 the region a concurrent influence on rainfall distribution. This suggests that ENSO can
 475 modulate or amplify the IOD signal when both phenomena occur simultaneously.
 476 Another noteworthy pattern emerges over the eastern equatorial Atlantic, where
 477 strong positive and significant regression values are observed (Fig. 5a). **A recent** study
 478 by Moihamette et al. (2024) shows that rainfall variability over the areas along the
 479 Atlantic coast during IOD events can be influenced by Atlantic SST anomalies through
 480 atmospheric bridge mechanisms. The model at both L0 and L1 successfully captures
 481 this Atlantic teleconnection. **The model at both L0 and L1 appears to successfully**
 482 **capture this Atlantic teleconnection.**



483

484 **Fig 5:** Same as Fig. 4, but for regression of the EA precipitation with the global SST. The black
 485 and green boxes indicate the IOD and N34 oceanic regions, respectively.

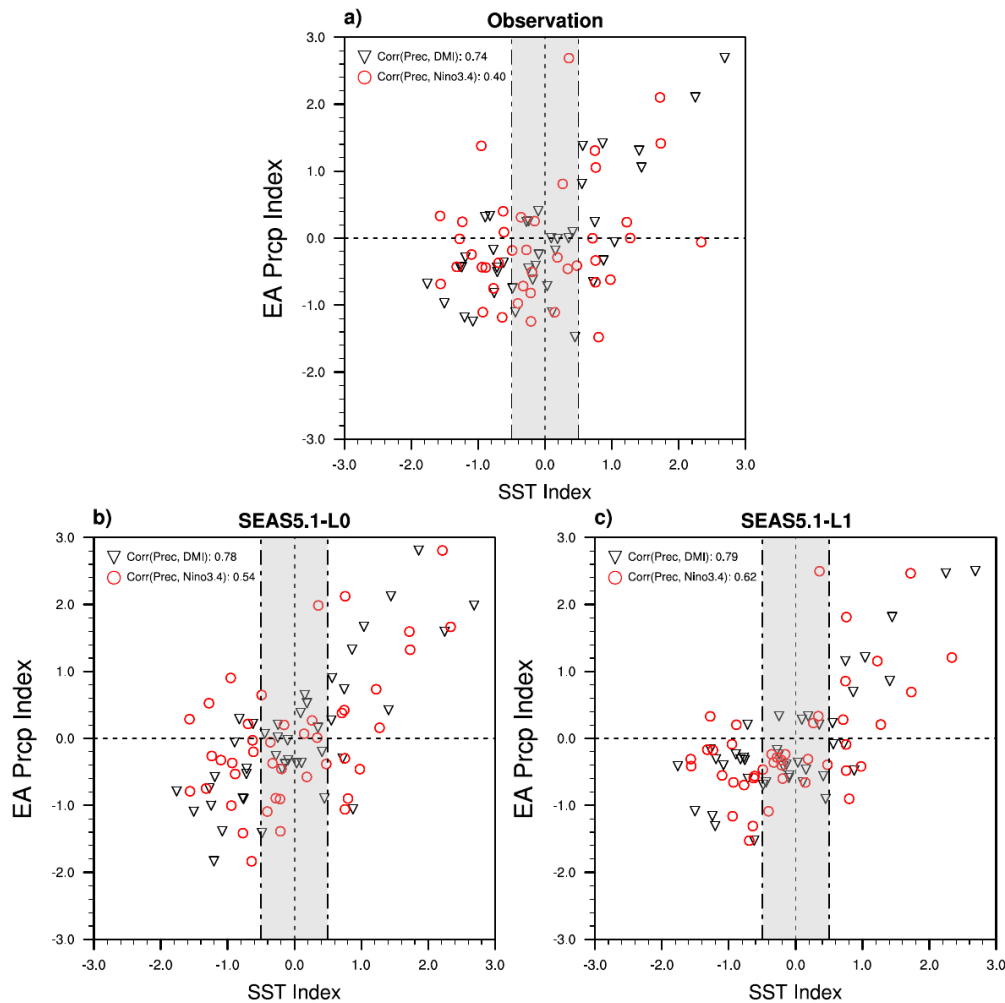
486

487 To further analyse the relationship between EA rainfall and both ENSO and IOD,
488 Figure 6a outlines the scatterplots of the observed EA rainfall with the IOD and N34
489 indices during the SON season. The relationship between the EA rainfall index and the
490 DMI (black triangles) as well as N34 index (red circles) is clearly positive and statistically
491 significant (at 95% confidence level) with correlations of 0.74 and 0.40, respectively.
492 This confirms that IOD could have an impact on the EA rainfall independently of ENSO.
493 Moreover, these outcomes suggest that ENSO has an indirect effect through IOD
494 conditions, but also a direct impact on EA precipitation through an atmospheric bridge
495 (Ibebuchi 2021; Roy and Troccoli 2024). The SEAS5.1 captures these relationships
496 reasonably well at both L0 and L1, but overestimated the correlations, mainly the
497 ENSO-EA precipitation relationship (Fig. 6b,c).

498 Following the assessment of SEAS5.1 in simulating rainfall characteristics and
499 their associated teleconnections with SST, the analysis is extended to a composite-
500 based approach. This complementary framework allows a more detailed examination
501 of the large-scale atmospheric and oceanic patterns associated with extreme rainfall
502 events over EA. In particular, composites of precipitation, SST, and low-level wind fields
503 are used to **characterise** the dominant circulation features and moisture transport
504 pathways linked to these extremes. This approach provides additional physical insight
505 into the mechanisms driving extreme rainfall beyond the skill-based evaluation of the
506 model.

507

508

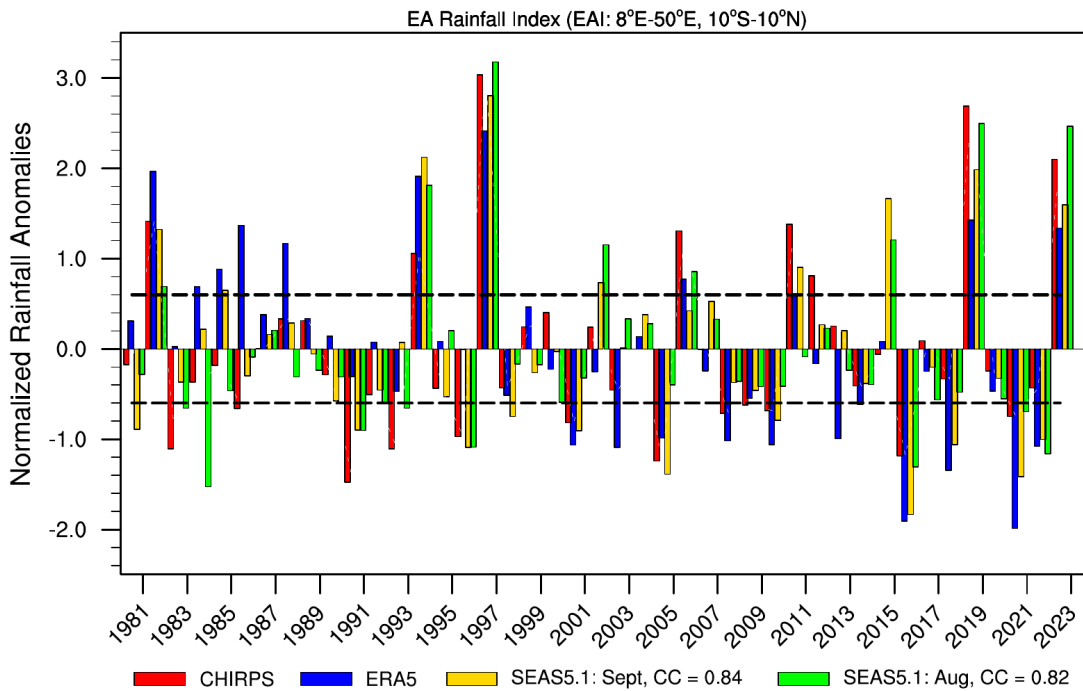


509

510 **Fig 6:** a) Observed Scatter plots for the EA precipitation with the DMI (black triangles) and N34
 511 (red open circles) and SST based indices for the SON season. **Note that the data points shown**
 512 **are ensemble mean values.** The grey shaded region corresponds to $\pm 0.5\sigma$ SST anomalies.
 513 Correlation Coefficient (CC) of EA precipitation index and DMI (N34) SST index is indicated at the
 514 top left of the map. (b) and (c) same as of panel (a) but for SEAS5.1 at L0 and L1, respectively.

515 **4. Extreme EA rainfall: composites analysis**

516 Firstly, we **computed** the time series of indices of standardised EA rainfall
 517 anomalies over the period 1981-2023 during SON season, for CHIRPS (red bar), ERA5
 518 (blue bar), and SEAS5.1 at L0 (gold bar) and L1 (green bar). The CC between CHIRPS and
 519 SEAS5.1 EA rainfall index at L0 and L1 is 0.84 and 0.82, respectively (statistically
 520 significant at the 99% confidence level). Using the criteria described in Sect. 2.2 to
 521 detect extreme rainfall, years with strong and weak rainfall over EA are defined.
 522 Thirteen extreme rainfall years have been highlighted (Fig. 7), including seven Strong
 523 Years (SY) and six Weak Years (WY). Table 1 **summarises** the different extreme rainfall
 524 years based on both CHIRPS and ERA5 rainfall. Six (Five) of observed SY (WY) are
 525 captured by the model at L0, whereas six (two) are captured at L1.



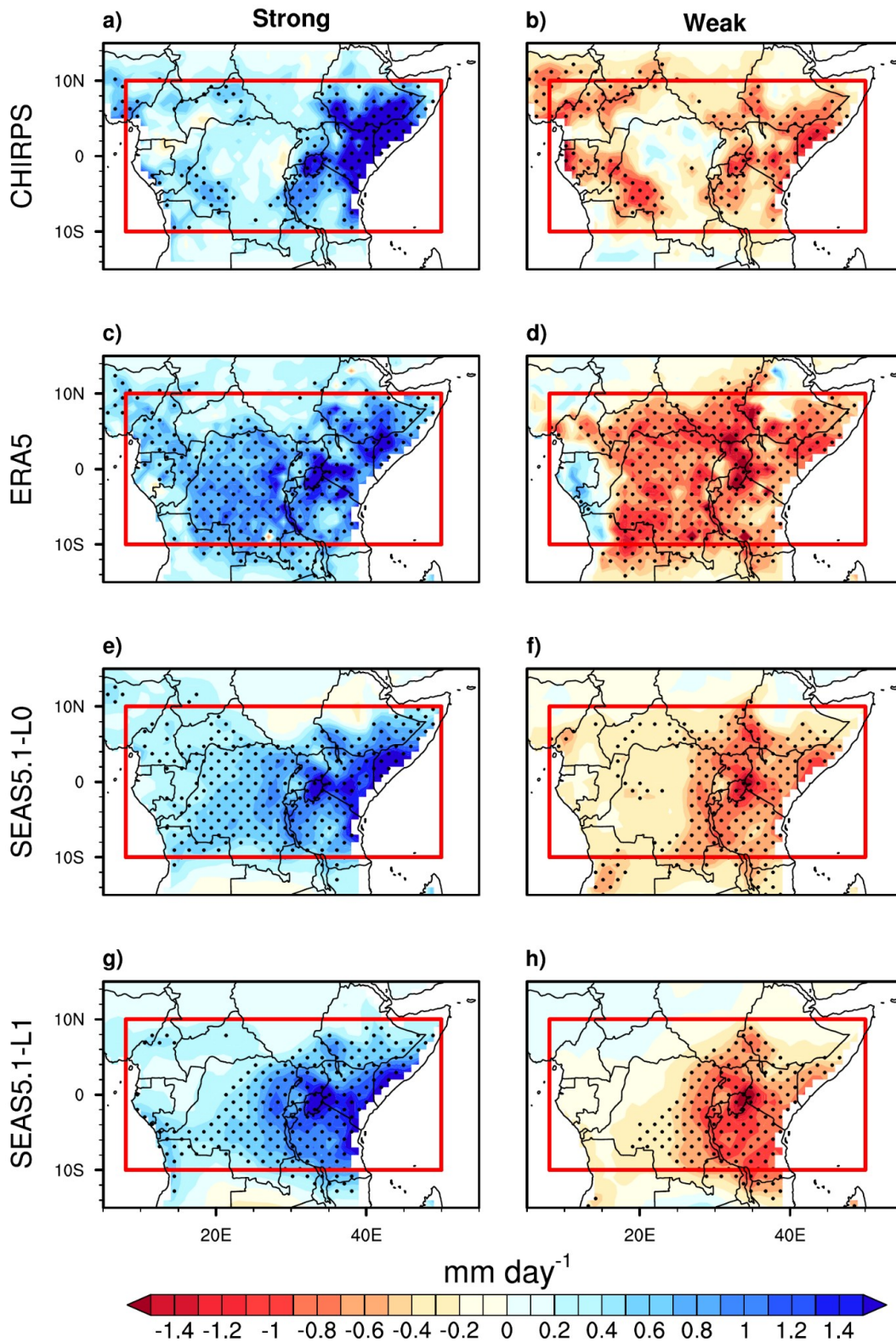
526

527 **Fig 7:** Indices of standardised EA rainfall anomalies over the period 1981-2023 during SON, for
 528 CHIRPS (red), ERA5 (blue), model at L0 (gold) and L1 (green). Dashed black line denotes ± 1
 529 standard deviation of seasonal anomalies. The CC value between observed and predicted EA
 530 rainfall is shown in the legend below the map.

531 **Table 1:** Strong and weak EA rainfall years used in this study

Category	Years
Strong Years (SY)	1982* [☒] , 1994* [☒] , 1997* [☒] , 2006 [☒] , 2011*, 2019* [☒] , 2023* [☒]
Weak Years (WY)	2001*, 2005*, 2008, 2010*, 2016* [☒] , 2021* [☒]

532 The asterisk (*) indicates the years captured by the model at L0, and the square (☒)
 533 those captured by the model at L1.



534

535 **Fig 8:** Composite of precipitation anomalies (in mm day⁻¹) during (first column) strong years and
 536 (second column) weak years from (a-b) CHIRPS, (c-d) ERA5 and SEAS5.1 [L0 (e-f) and L1 (g-h)].
 537 The red boxes indicate the EA region. The stippling occurs where the difference between the

538 composite and the mean climatology is locally statistically significant at the 95% confidence
539 level through the Student's t test

540 Figure 8 shows the composites of EA rainfall anomalies for SY (first column) and
541 WY (second column). It appears that during the observed SY composites (Fig. 8a,c),
542 eastern EA experienced significant positive rainfall anomalies, mainly over southern
543 Ethiopia and Somalia, as well as northern Kenya and Tanzania, where the IOD-rainfall
544 relationship was strongest (Fig. 4a). Over the western EA, the positive rainfall
545 anomalies are lower than over eastern EA, but are significant over certain areas
546 (southwest of DRC and eastern CAR), where the IOD-rainfall relationship was strongest
547 also. An opposite pattern is observed during the observed WY composites (Fig. 8b,d),
548 but with a weaker (stronger) anomalies magnitude over the eastern (western) part of
549 the EA, especially over Ethiopia, Kenya and Somalia (Cameroon, Gabon and DRC). **It is**
550 **important to note that ERA5 poorly represents precipitation anomaly values over**
551 **the central part of the domain, particularly over the DRC, compared to the CHIRPS**
552 **reference. This is explained by ERA5's low skill in these regions (Fig. S2).** These
553 observed characteristics of the rainfall composites are well simulated by the model at
554 L0 (Fig. 8e,f) as well as at L1 (Fig. 8g,f), but with a lower magnitude compared to
555 observations (mainly during WY composites; Fig. 8f,h). During the SY composite at L1
556 (Fig. 8g), the northern (southern) rainfall anomalies of eastern EA are underestimated
557 (overestimated), a similar pattern with the positive IOD-rainfall relationship over
558 eastern EA which shifted southwards at this Lead-time (Fig. 4c).

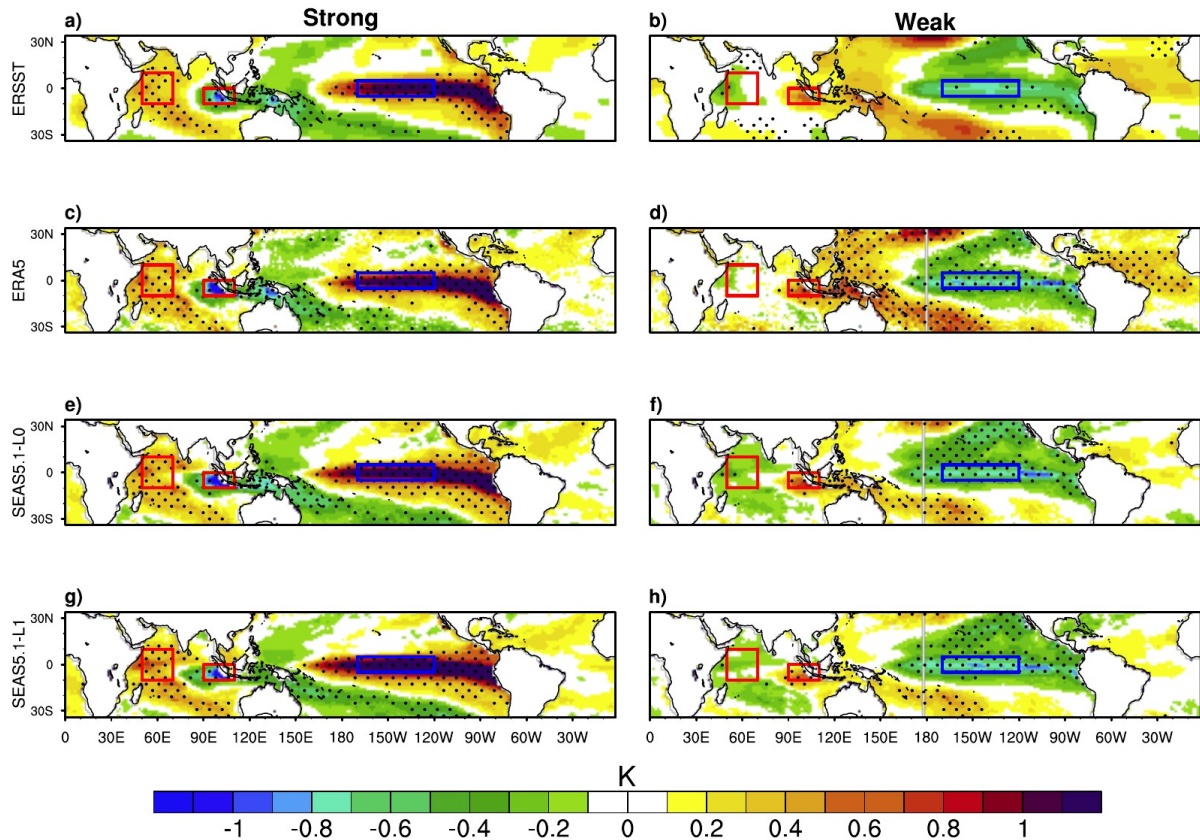
559

560 The monthly precipitation PDFs over EA during climatology mean (black line) SY
561 (blue line) and WY (red line) are further investigated using gamma distribution (Fig. S3).
562 The results confirm that more (less) observed/reanalysis rainfall are occurring over EA
563 region during SY (WY) composites, compared to the SON mean climatology (Fig. S3a,b).
564 These PDFs patterns were predicted successfully by SEAS5.1 at L0 (Fig. S3c) as well as at
565 L1 (Fig. S3d).

566 Previous studies highlighted the fact that spatial pattern of extreme rainfall over
567 EA is strongly influenced by SST anomalies in the surrounding ocean basins (Palmer et
568 al., 2023; Roy et al., 2024; Nana et al., 2023,2025). Examining the associated SST
569 composites therefore provides essential insight into the drivers of these rainfall
570 extremes, and highlights the importance of accurately representing oceanic conditions
571 in seasonal prediction models (Nana et al., 2024). To get an insight into the way SST
572 responds to extreme rainfall events over EA, the composites of global SST anomalies
573 for SY and WY events are presented in Fig. 9. As seen in Fig. 5, favourable conditions for
574 the occurrence of EA rainfall is associated with warming (cooling) of the SST over WIO
575 (EIO) areas (black boxes in Fig. 5), and warming of the SST over the ENSO region (green
576 boxes in Fig. 5). It appears that during observed SY composites (Fig. 9a,c), the IO shows
577 significant warming (cooling) of the SST located over WIO (EIO) while the area of
578 interaction of Niño-3.4 simultaneously exhibits strong and positive SST anomalies,

579 characterising El Niño events. An opposite pattern is observed during the WY years
580 (Fig. 9b,d). It should be noted that the EIO exhibits stronger SST anomalies than those
581 over the WIO, suggesting that IOD intensity is strongly modulated by the SST changes
582 over the EIO, as suggested by Cai et al. (2011). It is important to note that SST anomaly
583 values are stronger during the SY composites compared to those observed during WY
584 events. This can be explained by the fact that, among the seven SY years, three
585 correspond to El Niño record events (1982, 1997, 2023) and two to moderate events
586 (1994 and 2006), with six of them also coinciding with positive IOD episodes. In
587 contrast, among the six WY years, only one corresponds to a significant La Niña event
588 (2016) with four moderate events (2005, 2008, 2010, 2021), while four are associated
589 with moderate negative IOD episodes. These outcomes confirm that the anomalous
590 extreme rainfall which occurs over EA during the SON season are strongly associated
591 with SST anomalies over these two oceanic regions. The above results and conclusion
592 are in agreement with recent findings by Nana et al. (2025). The model predicted these
593 observed composite patterns well at L0 (Fig. 9e,f) and L1 (Fig. 9g,h). The observed SST
594 anomalies, as well as rainfall anomalies (Fig. 8) stronger during SY than during WY, are
595 well simulated by the model at these two Lead-time. During SY events, for both
596 initialization conditions, the model successfully captures the spatial distribution and
597 intensity of SST anomalies (Fig. 9e,g), which is consistent with its good performance in
598 reproducing the associated rainfall anomalies (Fig. 8e,g). In contrast, during WY events,
599 the model overestimates SST anomaly amplitudes across the three domains (Fig. 9f,h),
600 with the largest biases occurring in the western IOD box. This warm bias likely
601 contributes to more rainfall anomalies simulated by the model (Fig. 8f,h) compared to
602 observation (Fig. 8b). This finding is in line with Moihamette et al. (2024), who
603 demonstrated that the western IOD pole plays a dominant role in the IOD-precipitation
604 relationship over the region during the SON season.

605



606
607
608

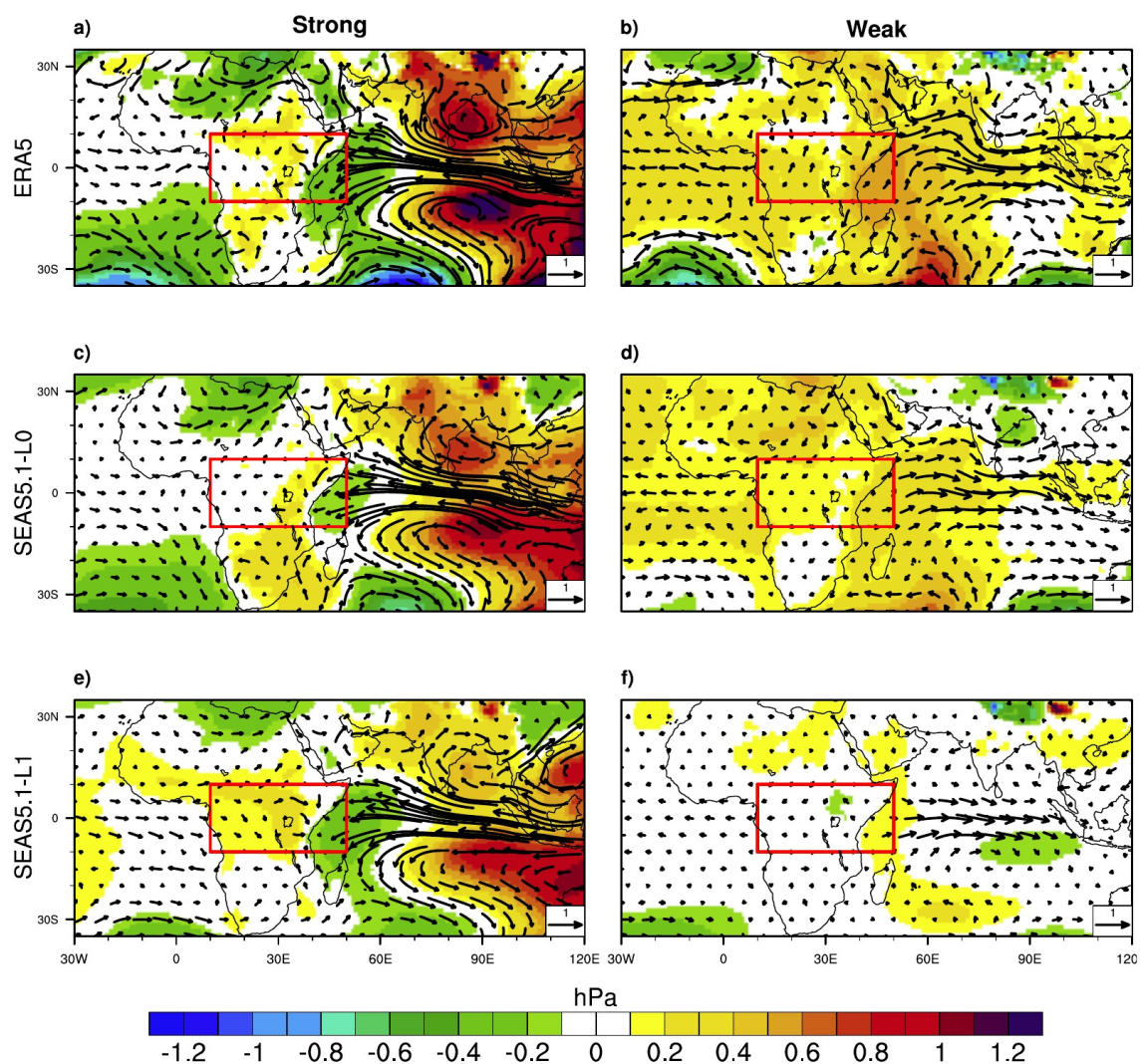
Fig 9: Same as in Fig. 8, but for SST (in K). The red and blue boxes indicate the IOD and N34 oceanic regions, respectively.

609

610 5. Atmospheric circulation: composites analysis

611 Previously, observed and reanalysis, as well as predicted composite SST
612 anomalies over the Atlantic, Indian, and Pacific oceans showed a strong and significant
613 composite anomalies pattern during both strong and weak years (but more
614 pronounced during SY than WY), which shows that EA rainfall has diverse dynamical
615 linkages from these oceanic regions. We are now interested in the large-scale control
616 of EA precipitation, as, following Nana et al. (2023, 2025) and Dezfuli and Nicholson
617 (2013), interannual variations in EA precipitation are strongly influenced by large-scale
618 climatic factors such as east Atlantic SST, IOD and ENSO. Figure 10 investigated the
619 model's ability to predict large-scale circulation patterns through horizontal wind at
620 850 hPa and MSLP. During SY (WY) composites, the eastern and western equatorial IO
621 experience strong easterly (westerly) wind anomalies, while eastern equatorial Atlantic
622 exhibits weak westerly wind anomalies (Fig. 10a,b). According to Moihamette et al.
623 (2024) and Nana et al. (2025), strong (weak) circulation patterns over the EA region are
624 predominant during excess (deficit) rainfall years as a result of large-scale circulations
625 from both equatorial Indian and eastern Atlantic oceans. These circulation patterns are
626 associated with dipole mode over IO, more pronounced during SY (Fig. 10a) than WY
627 (Fig. 10b), characterised by strong positive (negative) and significant values over EIO

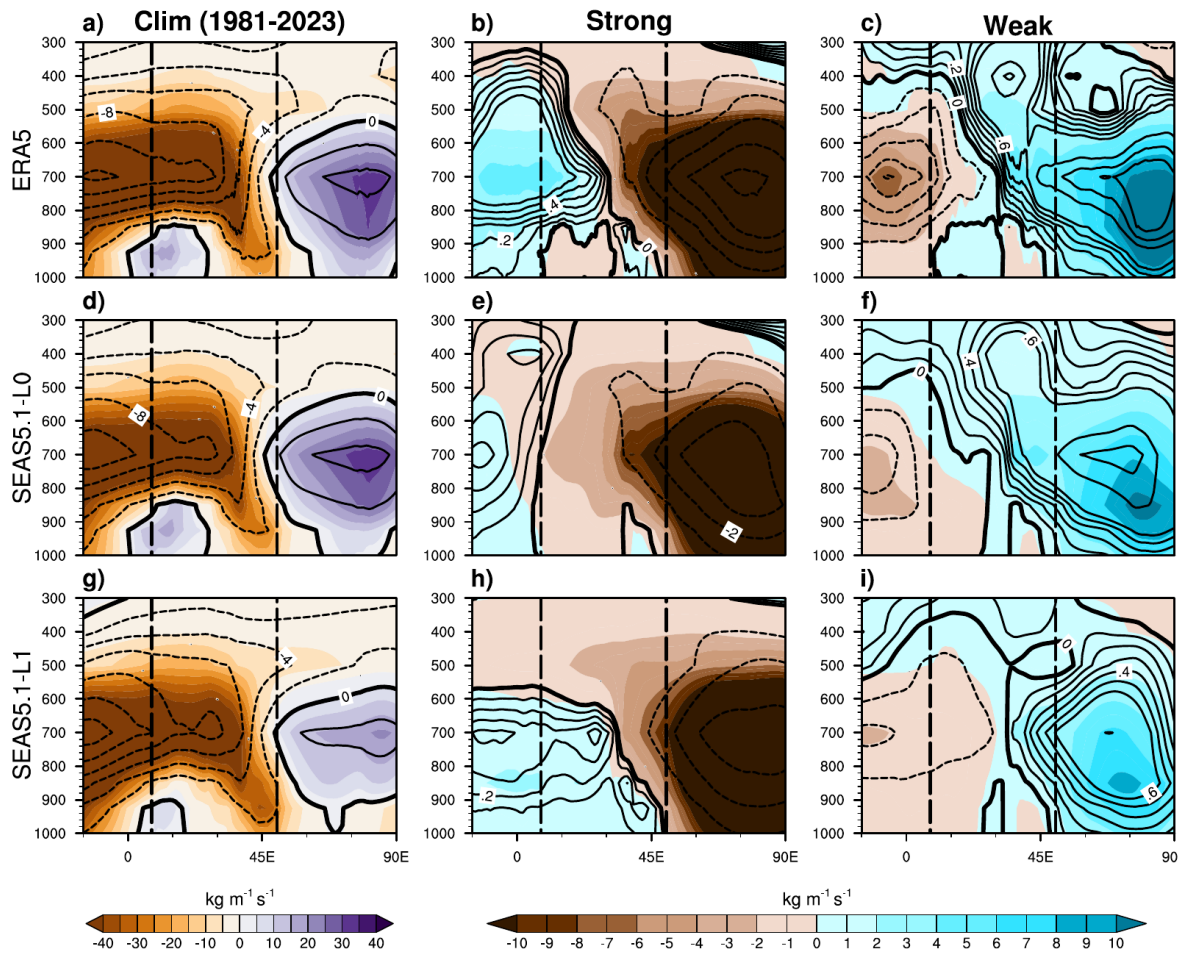
628 (WIO). Also, the southeast Atlantic coastal region exhibits negative composite
 629 anomalies (Fig. 10a). This is consistent with the work of Dezfuli and Nicholson (2013),
 630 who found that SY (WY) events over eastern EA are associated with negative (positive)
 631 MSLP anomalies over WIO (EIO), whereas negative (positive) MSLP anomalies over
 632 southeast Atlantic coast occur during SY (WY) events over western EA. These observed
 633 composite features are well predicted with the September IC (Fig. 10c,d) and August
 634 initial condition predictions (Fig. 10e,f). The MSLP anomalies are underestimated by the
 635 model during SY (WY) at L0 (L1), mainly over WIO (whole of the EA as well as oceanic
 636 areas). These changes in SST (Fig. 9), wind and MSLP (Fig. 10) during the two rainfall
 637 events appear to be contrasted mainly over Indian ocean (strongly over the equatorial
 638 IO) compared to the equatorial Atlantic, and according to Nicholson (2015) and Nana et
 639 al. (2025), are responsible for the moisture supply over the EA during SON season.



640

641 **Fig 10:** Same as in Fig. 8, but for MSLP (shading, in hPa) and 850 hPa wind (vector, m s^{-1}). The
 642 value higher (lower) than 0.02 (-0.02) hPa is locally statistically significant at 95% confidence
 643 level

645 To highlight the atmospheric layer responsible for the moisture surplus or
646 deficit over the region during the two extreme EA rainfall, we have examined in Figure
647 11 the vertical profile of the longitude-height cross-section of the observed and
648 predicted zonal moisture flux between 1000-300 hPa, overlaid by the zonal wind and
649 averaged between 10° S-10° N. The first column shows the SON mean climatology, the
650 second and third column show the strong and weak composite anomalies, respectively.
651 It emerges that the model successfully predicted the observed westerly climatology
652 moisture transport (first column) as well as westerly wind from Atlantic Ocean to
653 western EA in the lower troposphere (1000-850 hPa, **around 0°-15° E**). This observed
654 and forecast configuration in the lower troposphere over the eastern Atlantic Ocean
655 and western EA is the same as that observed 1000-550 hPa over the Indian Ocean.
656 However, we note an underestimation of both moisture flux (**shade in Fig. 11g**) and
657 wind at L1 (**dash and solid lines in** Fig. 11g). During SY (second column), anomalous
658 easterly moisture transport occurs from IO (**45° -90° E**; in total troposphere) to EA
659 (strong over middle troposphere in the eastern part), whereas the western part of EA
660 exhibited strong westerly moisture transport in the middle troposphere (850-600 hPa)
661 from the equatorial Atlantic ocean (Fig. 11b). In the lower troposphere (1000-850 hPa),
662 easterly moisture transport prevailed over the EA region, whereas a westerly
663 circulation appeared only in the mid-troposphere (850-600 hPa), with a weaker
664 intensity compared to that originating from the IO. The easterly moisture transport
665 anomalies over IO are well captured by the model (Fig. 11e,h). However, the model
666 overestimated (underestimated) the easterly (westerly) moisture transport **over east**
667 **(west) of 13° E** over the middle troposphere (850-600 hPa) at L0 (Fig. 11e), whereas an
668 **overestimation (underestimation)** of westerly (easterly) moisture transport featured
669 over western (eastern) EA **over west (east) of 30° E** between 1000-500 hPa at L1 (Fig.
670 11h). During WY (third column), observation (Fig. 11c) as well as model at L0 (Fig. 11f)
671 and L1 (Fig. 11i) shows westerly (easterly) moisture transport over the Indian (Atlantic)
672 ocean. Over western EA domain (**between 13° E and 30° E**), the model at L0 and L1
673 shows easterly moisture flux anomalies while observation shows westerly anomalies,
674 but underestimated the observed Atlantic eastern moisture transport. In addition,
675 anomalous westerly winds are weakened and easterly winds develop in the mid-
676 troposphere (at 700 hPa), **favouring** equatorial easterly moisture transport. We can
677 conclude that the two lead-time of the forecast model agree with two distinct
678 mechanisms controlling moisture transport, over the ocean and the continent.



679

680 **Fig 11:** Longitude-height cross-sections for (first column) mean climatology of SON 1981-2023,
 681 (second column) strong years composite anomalies and (third column) weak years composite
 682 anomalies of zonal moisture flux (shading, $\text{kg m}^{-1} \text{s}^{-1}$) and zonal wind (contour, m s^{-1}) for (a-c)
 683 ERA5, (d-f) L0 and (g-i) L1, averaged between 10°S - 10°N . The dashed black lines denote the
 684 limits of EA.

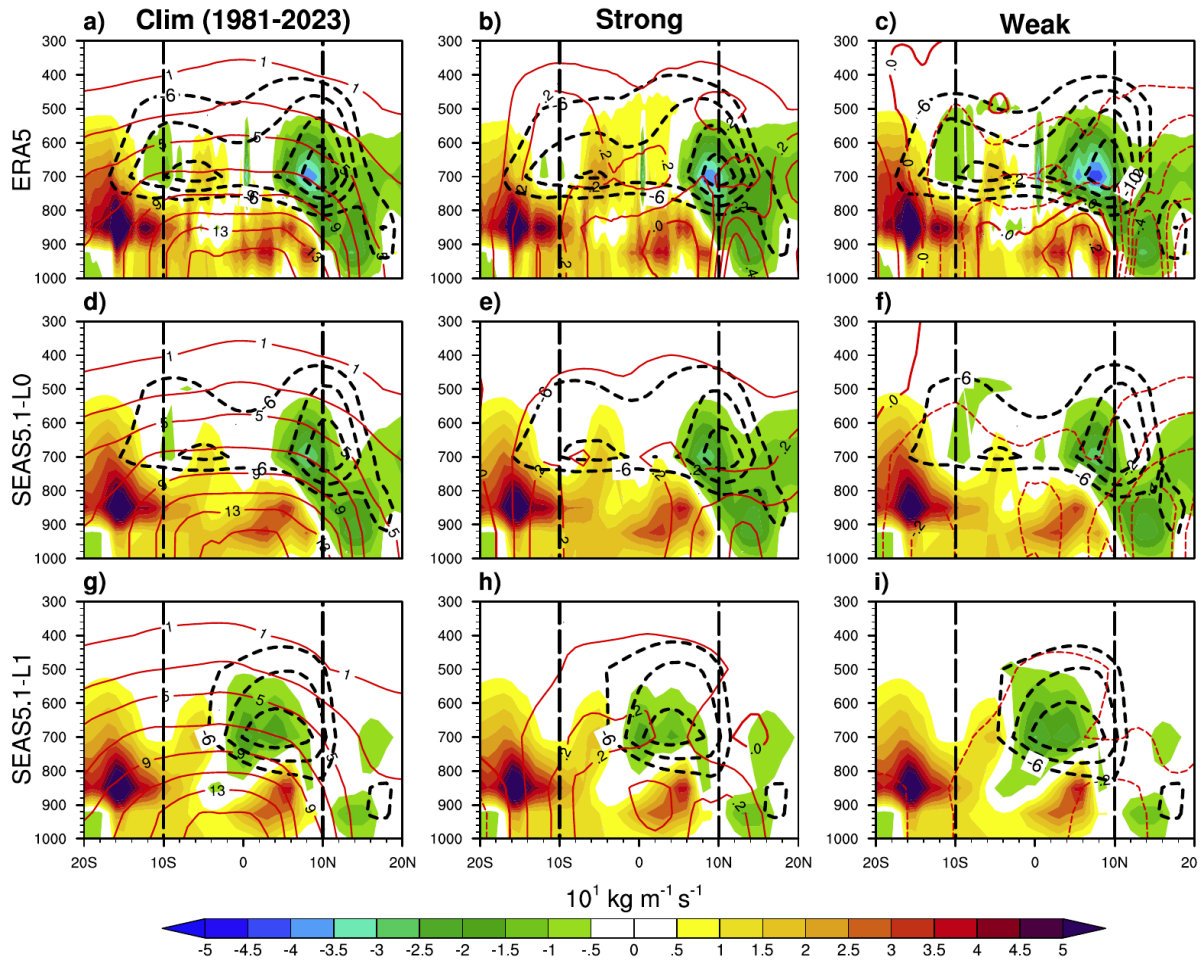
685

686 An important atmospheric feature over western East Africa is the African
 687 Easterly Jet (AEJ), defined as the maximum easterly winds in the mid-troposphere (700–
 688 600 hPa; Nicholson and Grist 2003). During the September–November rainfall season,
 689 the AEJ shows a southern branch (AEJ-S) with its core near 10°S , and a northern branch
 690 (AEJ-N), which occurs year-round with its core near 10°N (Kuethe et al., 2022). The
 691 following analysis highlights the characteristics of these features during extreme
 692 September–November rainfall episodes.

693 The Figure 12 evaluated the column stratification of atmospheric convergence
 694 through the latitude/height cross-sections of the net zonal moisture flux (shading)
 695 calculated from West boundary (10°E) minus East boundary (30°E) boundary of
 696 western EA over which the AEJ components (black dashed contours) at 15°E , and

697 specific humidity (red contours) calculated between 10°E and 30°, are overlaid. The first
698 column shows the SON mean climatology of three tools, the second column shows the
699 zonal moisture flux, AEJ and specific humidity composite anomaly for the SY
700 composites, as well as the third column, but for the WY composites. The findings by
701 Kuete et al. (2019) and Nicholson and Grist (2003) show that wet conditions over
702 western EA are associated with decrease of the **two** AEJ components through increase
703 in the middle tropospheric moisture convergence. Overall, the zonal net moisture flux
704 balance over the EA shows a different structure for climatology and composites
705 characterised by convergence in the middle troposphere (Fig. 12a-c) modulated by
706 both southern and northern AEJ components, AEJ-S and AEJ-N respectively. During SY
707 (Fig. 12b) composites, the AEJ-S and AEJ-N core **speeds decrease** compared to the
708 climatology (Fig. 12a), **leading to increase in moisture convergence over western EA**
709 **(between 10° S and 10° N) favouring wet conditions over western EA, whereas the**
710 **moisture divergence decreases at both 10° S and 10° N boundaries of EA favouring**
711 **dry conditions**, following Kuete et al. (2019) and Nicholson and Grist (2003). This
712 middle tropospheric moisture convergence is accompanied by positive specific
713 humidity anomalies. During WY (Fig. 12c) events, the two AEJ components are slightly
714 stronger compared to the climatology, resulting in a strong divergence at 10° S and
715 10° N boundaries, and a weak mid-tropospheric convergence that contributes to
716 intensified middle tropospheric divergence and followed by negative values of specific
717 humidity anomalies. A similar pattern is observed at L0 (Fig. 12d-f), but slightly
718 underestimated. Regarding the model at L1 (Fig. 12g-i), AEJ-N moves to the south, with
719 a core speed close to 5° N versus 10° N in observation as well as L0, accompanied by a
720 strong mid-tropospheric divergence leading to reduced mid-tropospheric
721 convergence. Another finding is the missing of the AEJ-S in climatology and both
722 composites.

723



724

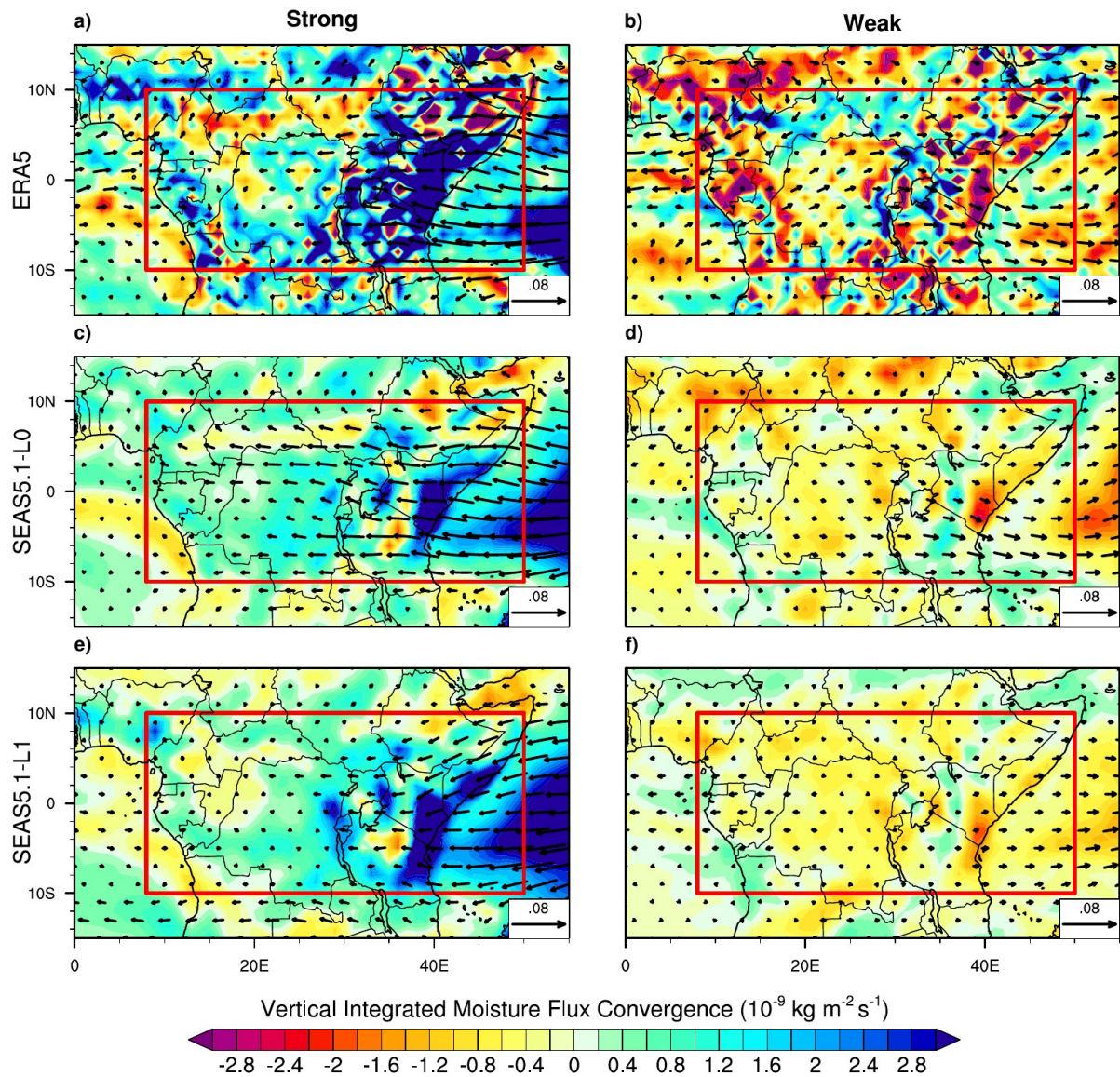
725 **Fig 12:** Latitude/height cross-sections of net zonal moisture flux (shading, $10^1 \text{ kg m}^{-1} \text{ s}^{-1}$)
 726 calculated from West boundary (10° E) minus East boundary (30° E) for (first column)
 727 climatology of SON 1981-2023 and (second column) strong years composite anomalies and
 728 (third column) weak years composite anomalies. Black dashed lines represent AEJ components
 729 ($U < -6 \text{ m s}^{-1}$) with the contour interval 2 m s^{-1} , calculated at 15° E for the respective periods. Red
 730 solid (dashed) lines represent SON mean climatology (composite anomalies) of specific humidity
 731 with the contour interval (first column) 2 Kg Kg^{-1} and (second and third column) 0.1 Kg Kg^{-1} ,
 732 averaged over $10^\circ\text{-}30^\circ \text{ E}$ for the respective periods. Positive values indicate moisture flux
 733 convergence, and negative values moisture flux divergence. The dashed black lines denote the
 734 limits of EA.

735

736 The vertically integrated moisture flux divergence (VIMFD) and vertically
 737 integrated moisture flux (VIMF) are important indicators of regions expected to receive
 738 rainfall. To provide a further exploration of the ability of ECMWF-SEAS5.1 forecasts to
 739 predict periods of heavy precipitation over the EA, we investigated the spatial patterns
 740 of both observed (Fig. 13a,b) and predicted (Fig. 13c,f) VIMFD anomalies over 1000-300
 741 hPa during SY and WY composites. SY (Fig. 13a) composite is characterised by an
 742 anomalous VIMF associated with easterly and westerly flux over WIO and eastern
 743 equatorial Atlantic, respectively. This moisture advection extends across the EA with

744 anomalous strong moisture convergence leading to wetter conditions over the region,
745 with highest moisture convergence anomaly values occurring over the eastern EA. An
746 opposite pattern feature during WY composite (Fig. 13b). Although underestimated,
747 the observed pattern is well predicted by the model at L0 (Fig. 13c-d) and L1 (Fig. 13e-f).
748 However, the model fails to simulate the westerly (easterly) flow over the Atlantic
749 Ocean during the SY (WY) composites at L0, in contrast to L1 where these flows are
750 represented, although underestimated by the model. Furthermore, examination of
751 Figures S4 and S5 confirms that moisture convergence is the main component of
752 moisture flux convergence, since, the spatial pattern of moisture convergence ($q\nabla\cdot V$) is
753 similar (and with the same strengths) to that of moisture flux convergence ($\nabla\cdot(qV)$), in
754 contrast to that of moisture advection ($V\cdot\nabla q$). This finding is in line with previous
755 research by Longandjo and Rouault (2023) and Kolstad et al. (2024), who show that
756 moisture convergence prevails in moisture flux convergence over western EA and
757 eastern EA, respectively. The model captures this moisture convergence very well as
758 the main component of moisture flux convergence (Kolstad et al., 2024) at L0 (Fig.
759 S4c,d and Fig. S5c,d) and L1 (Fig. S4e,f and Fig. S5e,f). In summary, precipitation in the
760 September and August IC predictions is reasonably represented, mainly driven by
761 dynamic processes from the IO, supporting the use of SEAS5.1 outputs for eastern EA
762 rainfall.

763



764

765 **Fig 13:** Same as Fig. 8, but for vertically integrated (1000-300 hPa) moisture flux (vectors, 10^{-9} kg
 766 $\text{m}^{-1} \text{ s}^{-1}$) and vertically integrated moisture flux convergence (positive values) or divergence
 767 (negative values) anomalies (shading, $10^{-6} \text{ kg m}^{-2} \text{ s}^{-1}$). Only locally significant vectors and shading
 768 above the 90 % level are shown. The red box indicates the EA region.

769

770

771

772

773

774

775 6. Summary and conclusions

776 By **analysing** hindcasts and forecasts from the latest operational seasonal
777 forecasting system based on dynamical climate models, the European Centre for
778 Medium-Range Weather Forecasts seasonal prediction system 5, version 5.1 (ECMWF-
779 SEAS5.1), this study highlights the influence of atmospheric drivers in forecasting
780 extreme precipitation events over EA during the September–October–November (SON)
781 season for the period 1981–2023. While some anomalous rainfall patterns over eastern
782 and western EA have been linked to moisture transport from the Indian and Atlantic
783 oceans respectively, further investigation is needed to evaluate the model’s ability to
784 simulate Madden–Julian Oscillation (MJO) activity during these extreme events.

785 The results indicate that the spatiotemporal and interannual variability of EA
786 rainfall is generally well represented by ECMWF-SEAS5.1 in both lead times during SON.
787 However, the model exhibits limited skill in predicting rainfall over the Congo Basin,
788 where hindcast data points are more dispersed at L0 than at L1, and both prediction
789 and confidence intervals deviate more strongly from the regression line at L0.
790 Predictability skill is higher for shorter lead times (September IC), particularly over
791 Kenya, southern Somalia, and northern Tanzania. Moreover, ECMWF-SEAS5.1
792 successfully reproduces large-scale teleconnections between tropical sea surface
793 temperatures over the Atlantic, Indian, and Pacific oceans and precipitation over EA,
794 with forecasts **initialised** in September (L0) showing stronger teleconnection skill than
795 those **initialised** in August (L1). For September ICs, the model captures 85.71% of
796 strong rainfall years and 83.3% of weak years, while for August ICs, it captures 85.71%
797 of strong years and 33.3% of weak years.

798 The model also demonstrates its ability to reproduce maximum composite
799 rainfall anomalies over eastern EA, particularly across Kenya, southern Ethiopia, and
800 Somalia, although it tends to underestimate their magnitude. Both the Indian Ocean
801 Dipole (IOD) and ENSO modes are realistically simulated during extreme events and for
802 both lead times, along with their associated atmospheric circulation. Furthermore,
803 ECMWF-SEAS5.1 accurately simulates moisture flux convergence and its components
804 (moisture convergence and moisture advection), with relatively stronger performance
805 for September IC compared to August. Overall, the system shows strong and
806 statistically significant skill in reproducing atmospheric features linked to extreme
807 rainfall events over EA, with higher performance in the eastern sector compared to the
808 western part. Given that skillful seasonal forecasting of equatorial rainfall has critical
809 socio-economic implications including reservoir management, groundwater recharge,
810 irrigation planning, and agricultural productivity these findings provide valuable
811 guidance for policymakers in the region to strengthen adaptation strategies and risk
812 mitigation efforts.

813

814

815 **Acknowledgements** The authors thank you to all reanalysis, observational, satellite
816 and hindcast data providers used in this study. We would like to express our gratitude
817 to the anonymous reviewers, along with the editor for their constructive suggestions,
818 which have greatly improved the quality of the paper. We gratefully appreciate the
819 efforts of the International Joint Laboratory Dynamics of Terrestrial Ecosystems in
820 Central Africa (IJL DYCOCA/ LMI DYCOFAC) initiative during the realisation of this work.

821 **Code availability** Figures shown in this study are plotted using the NCAR Command
822 Language (NCL; <https://doi.org/10.5065/D6WD3XH5>, NCAR Command Language,
823 2017). Codes can be obtained from the corresponding author.

824 **Author's contributions** **HNN**: Conceptualization; data upload; data analysis; formal
825 analysis; investigation; methodology; software; validation; writing-original draft;
826 writing-review and editing. **RST**: Project administration; supervision; validation;
827 methodology; writing; review and editing. **MG**: Project administration; supervision;
828 investigation; validation; writing-original draft; writing-review and editing. **DAV**: Project
829 administration; supervision; validation, methodology; writing; review and editing.

830 **Funding** Not applicable

831 **Data availability** All observational and reanalysis data used in this study are publicly
832 available at no charge and with unrestricted access. The ERA5 reanalysis is produced
833 within the Copernicus Climate Change Service (C3S) by the ECMWF and is accessible via
834 the link <https://cds.climate.copernicus.eu/datasets/>; the CHIRPS2 data are available at
835 https://data.chc.ucsb.edu/products/CHIRPS-2.0/global_daily/netcdf/; the ERSST data
836 are available at
837 <https://iridl.ldeo.columbia.edu/SOURCES/.NOAA/.NCDC/.ERSST/.version5/>. The ECMWF-
838 SEAS5.1 model data can be downloaded from the Copernicus Climate Data Store
839 ([https://cds.climate.copernicus.eu/datasets/seasonal-monthly-pressure-levels?
840 tab=download](https://cds.climate.copernicus.eu/datasets/seasonal-monthly-pressure-levels?tab=download))

841 **Conflict of interest** The authors declare no conflicts of interest relevant to this study.

842

843

844

845

846

847

848

849

850

851

852

853 **References**

- 854 Abid, M. A., Kucharski, F., Molteni, F., and Almazroui, M.: Predictability of Indian Ocean
855 precipitation and its North Atlantic teleconnections during early winter, *npj*
856 *Clim Atmos Sci* 6, 17 (2023), <https://doi.org/10.1038/s41612-023-00328-z>, 2022.
- 857 Attada, R., Ehsan, M. A., and Pillai, P. A.: Evaluation of potential predictability of
858 indian summer monsoon rainfall in ecmwf's fifth-generation seasonal forecast
859 system (SEAS5), *Pure Appl. Geophys.*, 179(12), 4639–4655,
860 <https://doi.org/10.1007/s00024-022-03184-9>, 2022.
- 861 Behera, S. K., Luo, J.-J., Masson, S., Delecluse, P., Gualdi, S., Navarra, A., and Yamagata,
862 T.: Paramount impact of the Indian Ocean dipole on the East African short
863 rains: A CGCM study, *J. Climate*, 18(21), 4514–4530,
864 <https://doi.org/10.1175/jcli3541.1>, 2005.
- 865 Cai, W., van Rensch, P., Cowan, T., and Hendon, H. H.: Teleconnection pathways of
866 ENSO and the IOD and the mechanisms for impacts on australian rainfall, *J.*
867 *Climate*, 24(15), 3910–3923, <https://doi.org/10.1175/2011jcli4129.1>, 2011.
- 868 Cook, K. H., and Vizy, E. K.: Hydrodynamics of regional and seasonal variations in
869 Congo Basin precipitation, *Clim. Dynam.*, 59(5–6), 1775–1797,
870 <https://doi.org/10.1007/s00382-021-06066-3>, 2021.
- 871 Dezfuli, A.: Climate of Western and Central Equatorial Africa. In *Oxford Research*
872 *Encyclopedia of Climate Science*. Oxford University Press,
873 <https://doi.org/10.1093/acrefore/9780190228620.013.511>, 2017.
- 874 Dezfuli, A. K., and Nicholson, S. E. : The relationship of rainfall variability in Western
875 Equatorial Africa to the tropical oceans and atmospheric circulation. Part II: The
876 Boreal Autumn, *J. Climate*, 26(1), 66–84,
877 <https://doi.org/10.1175/jcli-d-11-00686.1>, 2013.
- 878 Dinku, T., Funk, C., Peterson, P., Maidment, R., Tadesse, T., Gadain, H., and Ceccato, P.:
879 Validation of the CHIRPS satellite rainfall estimates over eastern Africa, *Quart. J.*
880 *Roy. Meteorol. Soc.*, 144(S1), 292–312, <https://doi.org/10.1002/qj.3244>, 2018.
- 881 Ehsan, M. A., Tippet, M. K., Robertson, A. W., Almazroui, M., Ismail, M., Dinku, T.,
882 Acharya, N., Siebert, A., Ahmed, J. S., and Teshome, A.: Seasonal
883 predictability of Ethiopian Kiremt rainfall and forecast skill of ECMWF's SEAS5
884 model, *Clim. Dynam.*, 57(11–12), 3075–3091,
885 <https://doi.org/10.1007/s00382021-05855-0>, 2021.
- 886 Feudjio Tchinda, A., Tanessong, R. S., Mamadou, O., Tchida Dikko, V., Djomou Yepdo, Z.,
887 and Chabi Orou, J. B.: Predictive skill of North American Multi-Model Ensemble
888 seasonal forecasts for the climate rainfall over Central Africa, *Meteorol. Appl.*,
889 29(3), <https://doi.org/10.1002/met.2074>, 2022.
- 890 Funk, C., Peterson, P., Landsfeld, M., Pedreros, D., Verdin, J., Shukla, S., Husak, G.,
891 Rowland, J., Harrison, L., Hoell, A., and Michaelsen, J.: The climate hazards

892 infrared precipitation with stations—a new environmental record for monitoring
893 extremes, *Sci. Data*, 2(1), <https://doi.org/10.1038/sdata.2015.66>, 2015.

894 Gebrechorkos, S. H., Pan, M., Beck, H. E., and Sheffield, J.: Performance of state-of-
895 the-art C3S european seasonal climate forecast models for mean and extreme
896 precipitation over africa, *Water Resour. Res.*, 58(3),
897 <https://doi.org/10.1029/2021wr031480>, 2022.

898 Gleixner, S., Demissie, T., and Diro, G. T.: Did ERA5 improve temperature and
899 precipitation reanalysis over east africa? *Atmosphere*, 11(9), 996,
900 <https://doi.org/10.3390/atmos11090996>, 2020.

901 Gudoshava, M., Nyinguro, P., Talib, J., Wainwright, C., Mwanthi, A., Hirons, L., de
902 Andrade, F., Mutemi, J., Gitau, W., Thompson, E., Gacheru, J., Marsham, J., Endris,
903 H. S., Woolnough, S., Segele, Z., Atheru, Z., and Artan, G.: Drivers of sub-
904 seasonal extreme rainfall and their representation in ECMWF forecasts during
905 the Eastern African March-to-May seasons of 2018–2020, *Meteorol. Appl.*, 31(5),
906 <https://doi.org/10.1002/met.70000>, 2024.

907 Gudoshava, M., Wainwright, C., Hirons, L., Endris, H. S., Segele, Z. T., Woolnough, S.,
908 Atheru, Z., and Artan, G.: Atmospheric and oceanic conditions associated
909 with early and late onset for Eastern Africa short rains, *Int. J. Climatol.*, 42(12),
910 6562–6578, <https://doi.org/10.1002/joc.7627>, 2022.

911 Gudoshava, M., Wanzala, M., Thompson, E., Mwesigwa, J., Endris, H. S., Segele, Z.,
912 Hirons, L., Kipkogei, O., Mumbua, C., Njoka, W., Baraibar, M., de Andrade, F.,
913 Woolnough, S., Atheru, Z., and Artan, G.: Application of real time S2S forecasts
914 over Eastern Africa in the co-production of climate services, *Clim. Services*, 27,
915 100319, <https://doi.org/10.1016/j.cliser.2022.100319>, 2022.

916 Hersbach, H., Bell, B., Berrisford, P., Hirahara, S., Horányi, A., Muñoz-Sabater, J., Nicolas,
917 J., Peubey, C., Radu, R., Schepers, D., Simmons, A., Soci, C., Abdalla, S., Abellan,
918 X., Balsamo, G., Bechtold, P., Biavati, G., Bidlot, J., Bonavita, M., ... Thépaut, J.:
919 The ERA5 global reanalysis, *Quart. J. Roy. Meteorol. Soc.*, 146(730), 1999–2049,
920 <https://doi.org/10.1002/qj.3803>, 2020.

921 Huang, B., Thorne, P. W., Banzon, V. F., Boyer, T., Chepurin, G., Lawrimore, J. H., Menne,
922 M. J., Smith, T. M., Vose, R. S., and Zhang, H.-M.: Extended reconstructed sea
923 surface temperature, version 5 (ersstv5): Upgrades, validations, and
924 intercomparisons, *J. Climate*, 30(20), 8179–8205,
925 <https://doi.org/10.1175/jcli-d-16-0836.1>, 2017.

926 Husak, G. J., Michaelsen, J., and Funk, C.: Use of the gamma distribution to represent
927 monthly rainfall in Africa for drought monitoring applications, *Int. J. Climatol.*,
928 27(7), 935–944, <https://doi.org/10.1002/joc.1441>, 2006.

929 Ibebuchi, C. C.: Revisiting the 1992 severe drought episode in South Africa: The
930 role of El Niño in the anomalies of atmospheric circulation types in Africa south
931 of the equator, *Theor. Appl. Climatol.*, 146(1–2), 723–740,

932 <https://doi.org/10.1007/s00704-021-03741-7>, 2021.

933 Ingeri, C., Wen, W., Sebaziga, J. N., Iyakaremye, V., Ekwacu, S., Ayabagabo, P.,
934 Twahirwa, A., and Kazora, J.: Potential driving systems associated with
935 extreme rainfall across East Africa during october to december (OND) season
936 2019, *Journal of Geoscience and Environment Protection*, 12(07), 25–49,
937 <https://doi.org/10.4236/gep.2024.127003>, 2024.

938 Johnson, S. J., Stockdale, T. N., Ferranti, L., Balmaseda, M. A., Molteni, F., Magnusson, L.,
939 Tietsche, S., Decremmer, D., Weisheimer, A., Balsamo, G., Keeley, S. P. E.,
940 Mogensen, K., Zuo, H., and Monge-Sanz, B. M.: SEAS5: The new ECMWF
941 seasonal forecast system, *Geosci. Model Dev.*, 12(3), 1087–1117,
942 <https://doi.org/10.5194/gmd-12-1087-2019>, 2019.

943 Kang, IS., and Shukla, J.: Dynamic seasonal prediction and predictability of the
944 monsoon. In: *The Asian Monsoon*, Springer Praxis Books. Springer, Berlin,
945 Heidelberg, https://doi.org/10.1007/3-540-37722-0_15, 2006.

946 Kenfack, K., Marra, F., Djomou, Z. Y., Tchotchou, L. A. D., Tamoffo, A. T., and Vondou, D.
947 A.: Dynamic and thermodynamic contribution to the October 2019 exceptional
948 rainfall in western central Africa, *Weather Clim. Dynam.*, 5, 1457–1472,
949 <https://doi.org/10.5194/wcd-5-1457-2024>, 2024.

950 Kolstad, E. W., and MacLeod, D. : Lagged oceanic effects on the East African short
951 rains, *Clim. Dynam.*, 59(3–4), 1043–1056,
952 <https://doi.org/10.1007/s00382-022-06176-6>, 2022.

953 Kolstad, E. W., Parker, D. J., MacLeod, D. A., Wainwright, C. M., and Hirons, L. C.:
954 Beyond the regional average: Drivers of geographical rainfall variability during
955 East Africa’s short rains, *Quart. J. Roy. Meteorol. Soc.*, 150(764), 4550–4566,
956 <https://doi.org/10.1002/qj.4829>, 2024.

957 Kuete, G., Pokam Mba, W., and Washington, R.: African Easterly Jet South: Control,
958 maintenance mechanisms and link with Southern subtropical waves, *Clim.*
959 *Dynam.*, 54(3–4), 1539–1552, <https://doi.org/10.1007/s00382-019-05072-w>, 2019.

960 Longandjo, G.-N. T., and Rouault, M.: On the structure of the regional-scale circulation
961 over Central Africa: Seasonal evolution, variability, and mechanisms, *J. Climate*,
962 33(1), 145–162, <https://doi.org/10.1175/jcli-d-19-0176.1>, 2020.

963 Longandjo, G.-N. T., and Rouault, M.: Revisiting the seasonal cycle of rainfall over
964 Central Africa, *J. Climate*, 37(3), 1015–1032, [https://doi.org/10.1175/jcli-d-23-](https://doi.org/10.1175/jcli-d-23-0281.1)
965 [0281.1](https://doi.org/10.1175/jcli-d-23-0281.1), 2024.

966 Moihamette, F., Pokam, W. M., Diallo, I., and Washington, R.: Response of regional
967 circulation features to the Indian Ocean dipole and influence on Central Africa
968 climate, *Clim. Dynam.*, 62(6), 1–21, <https://doi.org/10.1007/s00382-024-07251-w>,
969 2024.

- 970 Mwangi, E., Wetterhall, F., Dutra, E., Di Giuseppe, F., & Pappenberger, F.:
 971 Forecasting droughts in East Africa, *Hydrol. Earth Syst. Sci.*, 18(2), 611–620,
 972 <https://doi.org/10.5194/hess-18-611-2014>, 2014.
- 973 Nana, H. N., Gudoshava, M., Tanessong, R. S., Tamoffo, A. T., and Vondou, D. A.:
 974 Diverse causes of extreme rainfall in November 2023 over Equatorial Africa,
 975 *Weather Clim. Dynam.*, 6(3), 741–756, <https://doi.org/10.5194/wcd-6-741-2025>
 976 Nana, H. N., Tamoffo, A. T., Kaissassou, S., Djiotang Tchotchou, L. A., Tanessong, R. S.,
 977 Kamsu-Tamo, P. H., Kenfack, K., and Vondou, D. A.: Performance-based
 978 evaluation of NMME and C3S models in forecasting the June–August Central
 979 African rainfall under the influence of the South Atlantic Ocean Dipole, *Int. J.*
 980 *Climatol.*, 44(7), 2462–2483, <https://doi.org/10.1002/joc.8463>, 2024.
- 981 Nana, H. N., Tanessong, R. S., Tchotchou, L. A. D., Tamoffo, A. T., Moihamette, F., and
 982 Vondou, D. A.: Influence of strong South Atlantic Ocean Dipole on the
 983 Central African rainfall's system, *Clim. Dynam.*, 62(1), 1–16,
 984 <https://doi.org/10.1007/s00382-023-06892-7>, 2023.
- 985 Nicholson, S. E.: Long-term variability of the East African 'short rains' and its links to
 986 large-scale factors, *Int. J. Climatol.*, 35(13), 3979–3990,
 987 <https://doi.org/10.1002/joc.4259>, 2015.
- 988 Nicholson, S. E., and Grist, J. P.: The seasonal evolution of the atmospheric circulation
 989 over west africa and equatorial africa, *J. Climate*, 16(7), 1013–1030,
 990 [https://doi.org/10.1175/1520-0442\(2003\)016<1013:tseota>2.0.co;2](https://doi.org/10.1175/1520-0442(2003)016<1013:tseota>2.0.co;2), 2003.
- 991 Okoola R. E., Camberlin P., and Ininda J. M. : Wet periods along the East African Coast
 992 and the extreme wet spell of October 1997, *J. Kenya Meteorol. Soc.*, 2:67–83,
 993 (hal-00320637), 2008.
- 994 Palmer, P. I., Wainwright, C. M., Dong, B., Maidment, R. I., Wheeler, K. G., Gedney, N.,
 995 Hickman, J. E., Madani, N., Folwell, S. S., Abdo, G., Allan, R. P., Black, E. C. L., Feng,
 996 L., Gudoshava, M., Haines, K., Huntingford, C., Kilavi, M., Lunt, M. F., Shaaban, A.,
 997 and Turner, A. G.: Drivers and impacts of Eastern African rainfall variability,
 998 *Nat. Rev. Earth Environ.*, 4(4), 254–270,
 999 <https://doi.org/10.1038/s43017-023-00397-x>, 2023.
- 1000 Pokam, W. M., Bain, C. L., Chadwick, R. S., Graham, R., Sonwa, D. J., and Kamga, F. M. :
 1001 Identification of processes driving low-level westerlies in west equatorial africa,
 1002 *J. Climate*, 27(11), 4245–4262, <https://doi.org/10.1175/jcli-d-13-00490.1>, 2014.
- 1003 Pokam, W. M., Djiotang, L. A. T., and Mkankam, F. K.: Erratum to: Atmospheric water
 1004 vapor transport and recycling in Equatorial Central Africa through NCEP/NCAR
 1005 reanalysis data, *Clim. Dynam.*, 42(1–2), 553–553,
 1006 <https://doi.org/10.1007/s00382-013-1977-4>, 2013.
- 1007 Preethi, B., Sabin, T. P., Adedoyin, J. A., and Ashok, K.: Impacts of the ENSO Modoki

1008 and other Tropical Indo-Pacific Climate-Drivers on African Rainfall, *Sci.*
1009 *Rep.*, 5(1), <https://doi.org/10.1038/srep16653>, 2015.

1010 Rowell, D. P., Folland, C. K., Maskell, K., and Ward, N. M.: Variability of summer rainfall
1011 over tropical north Africa (1906-92): Observations and modelling, *Quart. J. Roy.*
1012 *Meteorol. Soc.*, 121(523), 669–704, <https://doi.org/10.1256/smsqj.52310>, 1995.

1013 Roy, I., and Troccoli, A.: Identifying important drivers of East African October to
1014 December rainfall season, *Sci. Total Environ.*, 914, 169615,
1015 <https://doi.org/10.1016/j.scitotenv.2023.169615>, 2024.

1016 Saha, S., Moorthi, S., Wu, X., Wang, J., Nadiga, S., Tripp, P., Behringer, D., Hou, Y.-T.,
1017 Chuang, H., Iredell, M., Ek, M., Meng, J., Yang, R., Mendez, M. P., van den Dool,
1018 H., Zhang, Q., Wang, W., Chen, M., and Becker, E.: The NCEP climate forecast
1019 system version 2, *J. Climate*, 27(6), 2185–2208,
1020 <https://doi.org/10.1175/jcli-d-12-00823.1>, 2014.

1021 Saji, N. H., Goswami, B. N., Vinayachandran, P. N., and Yamagata, T.: A dipole mode in
1022 the tropical Indian Ocean, *Nature*, 401(6751), 360–363,
1023 <https://doi.org/10.1038/43854>, 1999.

1024 Tanessong, R. S., Fotso-Nguemo, T. C., Kaissassou, S., Guenang, G. M., Komkoua
1025 Mbienda, A. J., Djotang Tchotchou, L. A., Tchinda, A. F., Vondou, D. A., Pokam, W.
1026 M., Igri, P. M., and Yepdo, Z. D.: Climate forecast skill and teleconnections on
1027 seasonal time scales over Central Africa based on the North American Multi-
1028 Model Ensemble (NMME), *Meteorol. Atmos. Phys.*, 136(3).
1029 <https://doi.org/10.1007/s00703-024-01018-y>, 2024.

1030 Tanessong, R. S., Igri, P. M., Vondou, D. A., Tamo, P. H. K., and Kamga, F. M.: Evaluation
1031 of probabilistic precipitation forecast determined from WRF forecasted
1032 amounts, *Theor. Appl. Climatol.*, 116(3–4), 649–659,
1033 <https://doi.org/10.1007/s00704-013-0965-2>, 2013.

1034 Tanessong, R. S., Vondou, D. A., Djomou, Z. Y., and Igri, P. M.: WRF high resolution
1035 simulation of an extreme rainfall event over Douala (Cameroon): A case study,
1036 *Model, Earth Syst. Environ.*, 3(3), 927–942,
1037 <https://doi.org/10.1007/s40808-017-0343-7>, 2017.

1038 Tefera, A. K., Liguori, G., Cabos, W., and Navarra, A.: Seasonal forecasting of East
1039 African short rains, *Sc. Rep.*, 15(1),
1040 <https://doi.org/10.1038/s41598-025-86564-0>, 2025.

1041 Trenberth, K. E.: The definition of El Niño, *Bull. Amer. Meteorol. Soc.*, 78(12), 2771–2777,
1042 [https://doi.org/10.1175/1520-0477\(1997\)078<2771:tdoen>2.0.co;2](https://doi.org/10.1175/1520-0477(1997)078<2771:tdoen>2.0.co;2), 1997.

1043 Wilks, D. S.: “The Stippling Shows Statistically Significant Grid Points”: How Research
1044 Results are Routinely Overstated and Overinterpreted, and What to Do about It,
1045 *Bull. Amer. Meteorol. Soc.*, 97(12), 2263–2273,
1046 <https://doi.org/10.1175/bams-d-15-00267.1>, 2016.